

## SPECTRAL AND PHOTOMETRIC DIAGNOSTICS OF GIANT PLANET FORMATION SCENARIOS

DAVID S. SPIEGEL<sup>1,2</sup>, ADAM BURROWS<sup>2</sup>

<sup>1</sup>Institute for Advanced Study, Princeton, NJ 08540 and

<sup>2</sup>Department of Astrophysical Sciences, Peyton Hall, Princeton University, Princeton, NJ 08544

*Draft version October 22, 2018*

### ABSTRACT

Gas-giant planets that form via core accretion might have very different characteristics from those that form via disk-instability. Disk-instability objects are typically thought to have higher entropies, larger radii, and (generally) higher effective temperatures than core-accretion objects. In this paper, we provide a large set of models exploring the observational consequences of high-entropy (hot) and low-entropy (cold) initial conditions, in the hope that this will ultimately help to distinguish between different physical mechanisms of planet formation. However, the exact entropies and radii of newly-formed planets due to these two modes of formation cannot, at present, be precisely predicted. It is possible that the distribution of properties of core-accretion-formed planets and the distribution of properties of disk-instability-formed planets overlap. We, therefore, introduce a broad range of “Warm Start” gas-giant planet models. Between the hottest and the coldest models that we consider, differences in radii, temperatures, luminosities, and spectra persist for only a few million to a few tens of millions of years for planets that are a few times Jupiter’s mass or less. For planets that are  $\sim$ five times Jupiter’s mass or more, significant differences between hottest-start and coldest-start models persist for on the order of 100 Myrs. We find that out of the standard infrared bands ( $J$ ,  $H$ ,  $K$ ,  $L'$ ,  $M$ ,  $N$ ) the  $K$  and  $H$  bands are the most diagnostic of the initial conditions. A hottest-start model can be from  $\sim$ 4.5 magnitudes brighter (at Jupiter’s mass) to  $\sim$ 9 magnitudes brighter (at ten times Jupiter’s mass) than a coldest-start model in the first few million years. In more massive objects, these large differences in luminosity and spectrum persist for much longer than in less massive objects. Finally, we consider the influence of atmospheric conditions on spectra, and find that the presence or absence of clouds, and the metallicity of an atmosphere, can affect an object’s apparent brightness in different bands by up to several magnitudes.

*Subject headings:* planetary systems – radiative transfer – stars: low-mass, brown dwarfs – stars: evolution

### 1. INTRODUCTION

Objects in the giant planet and brown dwarf mass ranges probably form in at least two main ways. On theoretical grounds, core accretion seems necessary to explain planets like Jupiter and Saturn (Pollack et al. 1996), while direct gravitational collapse via disk instability might be unavoidable for objects that form more than several tens to hundreds of AU from their stars (Rafikov 2007; Kratter et al. 2010; Rafikov 2011). If the different modes of formation lead to different initial planet properties (such as heat content, radius, temperature, etc.) then there should be observables that, in principle, could be used to determine the mode of formation of giant planets and brown dwarfs (Fortney et al. 2005; Marley et al. 2007; Fortney et al. 2008).

Ambitious observing programs for the next decade hope to distinguish between core-accretion and disk-instability objects. Examples of such campaigns include the Gemini Planet Imager (GPI, Macintosh et al. 2006; McBride et al. 2011),

the Near-Infrared Coronagraphic Imager (NICI) on Gemini South (Liu et al. 2010), the Spectro-Polarimetric High-contrast Exoplanet REsearch instrument (SPHERE) on the Very Large Telescope (Beuzit et al. 2008), the Strategic Exploration of Exoplanets and Disks (SEEDS) experiment on Subaru (Tamura 2009; Janson et al. 2011b), and Project 1640 on Palomar (Hinkley et al. 2008, 2011). When low-mass stars and brown dwarfs occur in close binaries, dynamical mass estimates can be derived, which can then be used to inform the initial conditions employed in theoretical models (Konopacky et al. 2010). It might be very difficult to obtain similar mass estimates for directly imaged (wide-separation) planetary-mass binary companions to stars. Nevertheless, spectra or multiband imaging of young planets, together with estimates of the ages of the systems in which they are found, might be sufficient to derive constraints on both masses and initial conditions simultaneously.

Several authors have explored ways to observationally discriminate between different formation scenarios. Marley et al. (2007, hereafter M07) exam-

ined the photometric signatures of “hot start” and “cold start” formation scenarios. In their framework, the hot-start objects represent disk-instability planets and the cold-start ones represent those that form via core accretion. Fortney et al. (2008) examined the spectral signatures that distinguish this particular set of “hot-start” and “cold-start” models, and the influence of metallicity on emergent spectra.<sup>1</sup>

In this paper, we build on previous work by examining the photometric and spectral signatures of a wide range of initial conditions, and the influence on spectra of different atmosphere types. Because it is not clear what precise initial conditions ought to be expected for either the core accretion or the disk instability mode of formation, we introduce a class of “warm-start” models. It is possible that both the core accretion and the disk instability modes of formation produce initial conditions that span a range, with disk instability forming planets generally – but not always – larger, hotter, and having higher entropies. Our warm-start models, then, might be representative of possible outcomes of either mode of formation. In §2, we describe the dependence of planetary radius on mass and entropy, and the range of expected initial radii and entropies as a function of mass. In §3, we describe the cooling and shrinkage of young objects with a range of masses and initial entropies. In §4, we discuss the evolution of hot- and cold-start planet models. In §5, we present a continuum of warm-start models and discuss how observations could be used to constrain mass, initial entropy/radius, and atmosphere. Finally, in §6, we summarize our conclusions.

## 2. FORMATION SCENARIOS

There are two main ideas about how objects form in the mass range of giant planets and brown dwarfs (from a fraction of Jupiter’s mass –  $M_J$  – to tens of  $M_J$ ).<sup>2</sup> One is that solid cores, similar to, or somewhat more massive than, the terrestrial planets, form first, and then a runaway process of gas accretion follows. In this picture, once a solid core of  $\sim 10$  Earth masses has developed, the rate at which it accretes “atmosphere” increases dramatically. Surrounding

<sup>1</sup> An alternative potential observational discriminant between formation scenarios is related to the metallicity of stars where directly imaged giant planets are found. Giant planets in the inner few AU around their stars presumably formed via core accretion, and these objects seem to occur more frequently around more metal-rich stars (Fischer & Valenti 2005; Johnson et al. 2010). Crepp & Johnson (2011), therefore, suggest that finding a similar correlation between planet occurrence and metallicity for more distant (directly imaged) objects might provide evidence that they form via core accretion, as well.

<sup>2</sup> Planets are often distinguished from brown dwarfs via the deuterium-burning criterion, often said to be  $\sim 13$  Jupiter masses (Burrows et al. 1997, 2001; Chabrier & Baraffe 2000; Chabrier et al. 2005). However, this mass depends on metallicity, helium fraction, the presence or absence of clouds etc. (Saumon & Marley 2008; Spiegel et al. 2011). Mode of formation is arguably a better, albeit less readily observable, taxonomical discriminant (Burrows et al. 2001; Chabrier et al. 2005; Spiegel et al. 2011; Schneider et al. 2011).

gas from the disk flows inward and forms an accretion shock near the boundary of the growing planet. This shock can be quite luminous (Hubickyj et al. 2005; Marley et al. 2007), and might allow the infalling gas to radiate away much of its initial heat. Some recent observational work (e.g., Janson et al. 2011a) suggests that core accretion is indeed the predominant mode of planet formation. The other idea is that the protoplanetary disk becomes gravitationally unstable and collapses into fragments, forming planets directly. The former idea, called “core accretion” or “nucleation instability,” was suggested more than three decades ago (Harris 1978; Mizuno et al. 1978; Mizuno 1980), and has been further developed more recently (e.g., Ikoma et al. 2000, 2001). The second idea, called “disk instability,” has existed for at least six decades (Kuiper 1951). In recent years, this mechanism, which remains controversial in the inner  $\sim 10$  AU of a planetary system (Rafikov 2005), has been advocated largely by Boss (2000, 2007, 2010) and Mayer et al. (2002, 2004).

One obvious difference between the mechanisms is that core accretion involves accretion onto a core. This could lead objects that form through core accretion to have higher bulk metallicity than those that form through disk instability. Higher metallicity has two competing effects. For a given bulk entropy, it causes an object to have a smaller radius (Burrows et al. 2000; Guillot et al. 2006; Lecointe et al. 2009; Ibgui et al. 2010). However, it also leads to greater atmospheric opacity, which retards the rate at which an object cools and loses its initial entropy (Burrows et al. 2007).

A second difference between core accretion and disk instability has to do with the timescale of formation. Core accretion involves two distinct steps – the formation of a rocky core, and the subsequent accretion of gas. Simulations suggest that these processes take on the order of several to tens of millions of years (Pollack et al. 1996; Hubickyj et al. 2005). Core accretion simulations of the formation of Jupiter by Pollack et al. (1996) and Lissauer et al. (2009) indicate that the formation timescale depends sensitively on the areal surface density ( $\sigma_{\text{init}}$ ) of the protoplanetary disk. The Pollack et al. (1996) simulations indicate that the time required to form Jupiter is of order several million years (although for different values of  $\sigma_{\text{init}}$  the formation timescale can vary by an order of magnitude). The opacities of grains in the protoplanetary nebula can also have an important influence on the core-accretion formation process (Movshovitz et al. 2010). Direct collapse, on the other hand, is thought to proceed on an orbital timescale or a small multiple thereof – orders of magnitude faster than core accretion (Boss 2000).

A final difference involves the heat of formation that remains in the object once it is fully formed. The specific entropy of gas in the protoplanetary disk is quite high compared with that of a bound object, such as a planet or a brown dwarf. But how

much of its initial entropy does the gas lose in becoming part of such an object? In the core-accretion scenario, it is thought that an accretion disk forms with an accretion shock near the planet’s boundary (Hubickyj et al. 2005). As gas flows through the luminous accretion shock, it loses much of its initial entropy. For instance, in work by Hubickyj et al. (2005) and M07, the gas is assumed to accrete at the entropy of the atmosphere of the forming protoplanet; i.e., it is taken to lose all its initial (excess) entropy. Core accretion is sometimes, therefore, referred to as a “cold start” mechanism. In contrast, it is thought that disk instability leads gas to retain much more of its initial entropy, thus leading to the “hot start” appellation. For a given isolated object, a difference in initial entropy is observationally similar to a difference in age (the time required to cool from the high entropy condition to the low entropy condition). If the age of an object is known precisely enough, therefore, it might be possible to distinguish a cold start from a hot start based on the apparent current entropy (and observables that it influences, such as radius, effective temperature, luminosity, and spectrum). Since the relative precision with which age must be determined to make such a discrimination increases with increasing age, younger objects are far more useful than older objects for testing formation models.

The truth, however, might be somewhat more complicated than the simple “cold-start”/“hot-start” idea just presented. M07 pointed out that the exact post-accretion luminosity of core-accretion objects depends on uncertain details of the accretion process; however, they emphasize that there should be a large separation between the initial entropies of core-accretion planets and disk-instability planets. This conclusion might turn out to be true, but is perhaps not yet definitively established. The accretion shock of the core-accretion scenario might not be 100% efficient in removing the initial entropy (Bromley & Kenyon 2011; Mordasini et al. 2011). Conversely, an accretion shock might form in the disk-instability scenario as well, radiating away a significant amount of an object’s initial heat. In other words, the cold start might not be as cold as previously thought, nor the hot start as hot. In principle, this could lead to a spectrum of “warm start” initial conditions. Nevertheless, there are generally thought to be some broad differences between the early properties of objects that form via core accretion and those that form via disk instability. The infalling gas initially has a significant excess specific entropy relative to the atmosphere of the forming planet onto which it is accreting. If this infalling gas retains some of its initial excess entropy, the initial entropy of a newly-formed planet would depend on this (unknown) fraction. If, on the other hand, the gas radiates away all its initial entropy down to the entropy of the gas that is already present in the protoplanet, the object’s entropy at the conclusion of the accretion process depends on the (unknown) entropy of the gas that was already present. In either case, there is not an unam-

biguous prediction for the initial entropy of a “cold start” object that forms via core accretion.

In order to explore the range of initial entropies that are reasonable within the core-accretion context, we have computed a large number of new evolutionary models. We employ the boundary conditions of Burrows et al. (1997), and we assume with M07 that the infalling gas radiates until it is at the same entropy as the gas already present. Figure 1 displays our new models and the M07 ones. The thick yellow bands in the top (entropy) and bottom (radius) panels represent so-called “hot-start” models, whose initial entropies range between those of M07 (open circles) and the mustard-colored curve (in the top panel) that represents our “hottest-start” model. The blue bands in each panel represent “cold-start” models, bounded by a pair of our new core-accretion models (“Acc:  $3 \times 10^{-5}$ ” and “Acc:  $3 \times 10^{-6}$ , Z:  $10^{-2}$ ”, respectively). The various new core-accretion models are described in §4.1.

### 2.1. *The Influence of Radiating Efficiency During Formation*

Different model assumptions about the process of accretion influence the properties of newly-formed model planets. We, therefore, consider a range of assumed radiating efficiencies of the accretion shock. Bromley & Kenyon (2011) and Kenyon & Bromley (2011 in prep.) quantify this efficiency as  $1 - \eta$ , where  $\eta$  is the fraction of accretion energy that a parcel of gas retains when it hits the planet’s photosphere, and Kenyon (2011, private communication) has provided us with several models of forming planets with various values of  $\eta$ . We estimate the specific entropies of these model planets by finding the values of specific entropy that best explain (within the context of the Burrows et al. 1997 models) their combinations of mass, radius, and luminosity. These models used  $\eta$  values of 0.15, 0.35, 0.50, and 0.75. The three models with a low value of  $\eta = 0.15$  (which is, nevertheless, larger than the implied  $\eta$  value of 0 in both the M07-clone models and our newly calculated core-accretion models presented in Fig. 1) span the mass range from  $0.43 M_J$  to  $4.4 M_J$ , and for these, we infer specific entropy values from 5.2 to 6.3. These and all subsequent specific (per-baryon) entropy values are in units of Boltzmann’s constant per baryon. For comparison, Jupiter has a specific entropy of  $\sim 6$ . Though it might initially be surprising that newly formed planets should appear as cold as Jupiter is at  $\sim 4.5$  billion years, the differences between the equation of state (EOS) used in the Bromley & Kenyon (2011) models and the one (Saumon et al. 1995) used in both the M07 models and in our own might explain this apparent mystery. Since Bromley & Kenyon (2011) assume that infalling gas retains 15% of its excess internal energy, we presumably would have inferred a specific entropy closer to 9 (for reasons discussed below) if they had used the Saumon et al. (1995) EOS.

It is particularly instructive to examine the effect

of larger  $\eta$ . Inferring the specific entropy from mass and radius as before, we estimate that a  $0.88 M_J$  object formed with  $\eta = 0.35$  has a specific entropy of 7.5; a  $1.2 M_J$  object formed with  $\eta = 0.50$  has a specific entropy of 10.1; and a  $1.6 M_J$  object formed with  $\eta = 0.75$  has a specific entropy of 10.6. Given that the  $\eta = 0.15$  objects appeared to be roughly 3 units lower in specific entropy than the cold-start band in Fig. 1 (encompassing our own models and those of Marley et al. 2007), these specific entropy values at larger values of  $\eta$  might similarly be reduced below what our models would calculate if embedded in the same formation scenario. Specific entropy is, of course, not linearly additive, and so the 10.6 value cannot be adjusted upwards in a simple way. Still, this suggests that if the gas cools fairly inefficiently while falling onto a forming giant planet, the final assembly might be significantly hotter than core accretion models typically assume.

## 2.2. Evidence for Hot Starts?

Indeed, there is mounting evidence that suggests that particularly massive young objects form fairly hot. Several years ago, the brown dwarf eclipsing binary 2MASS J05352184-0546085 was discovered. The two objects in this system have masses  $57 M_J$  and  $36 M_J$ , and are thought to be quite young, less than a few million years old (Stassun et al. 2006, 2007). Their radii ( $6.5 R_J$  and  $5.0 R_J$ , respectively, where  $R_J$  is Jupiter’s radius) and effective temperatures (2650 K and 2790 K, respectively) are indicative of the high-entropy initial conditions expected in the case of direct gravitational collapse. The masses and orbits of the objects in this system are more reminiscent of very low-mass binary stars than of a star-planet system, and so the formation process might be expected to be more similar to star formation than to core accretion (Joergens 2008).

Observations suggest that some lower mass objects also form hot. For instance, the planets found in the HR8799 system (Marois et al. 2008, 2010) appear to be inconsistent with classical “cold start” models (Dodson-Robinson et al. 2009; Bowler et al. 2010; Janson et al. 2010; Currie et al. 2011; Madhusudhan et al. 2011). The planetary companion to  $\beta$ -Pictoris ( $\beta$ -Pic b) also appears to have formed hotter than cold-start models would have predicted (Lagrange et al. 2010; Quanz et al. 2010). Other young substellar objects, such as GQ Lupi b, can similarly inform our understanding of the character of their geneses and early evolution (McElwain et al. 2007; Neuhäuser et al. 2008). Given both the theoretical prejudice against disk instability as the dominant mode of giant planet formation and the recent observational evidence that objects do not form as cold as some core-accretion models suggest, the time is ripe to revisit what observations can tell us about the properties of very young planets.

## 3. EVOLUTIONARY COOLING

As a self-gravitating sphere ages, it cools and shrinks. The cooling is rapid at first, and slows as the object reaches lower effective temperatures. More massive objects retain their heat for longer, since their gravitational energy scales with  $M^2$  (and by Virial equilibrium, the thermal energy scales with the gravitational energy).

Figure 2 vividly portrays how the cooling time scales with mass and with initial entropy, for Burrows et al. (1997) models. For objects of 1, 3, 10, and 15 times Jupiter’s mass, we plot the time required to reach various threshold specific entropies (10, 11, and 12), as a function of the object’s initial entropy.  $15-M_J$  objects require several tens of Myr to cool to  $S = 10$  (where  $S$  is specific entropy, in units of Boltzmann constant per baryon), several Myr to cool to  $S = 11$ , and about 1 Myr to cool to  $S = 12$ . Less massive objects cool to  $S = 10$  in a few Myr or less. Objects up to  $10 M_J$  cool to an entropy of 12 extremely quickly (in less than a million years after “formation” – the end of accretion), irrespective of initial entropy. Reaching an entropy of 11 takes a factor of several longer ( $\sim 2$  Myr for  $10-M_J$  models that start very hot). Reaching an entropy of 10 takes  $10-M_J$  models  $\sim 5$  Myr. The cooling times are a factor of  $\sim 4$  less for  $3-M_J$  models and another factor of  $\sim 3$  less for  $1-M_J$  models.

As an object loses entropy, its radius shrinks. Figure 3 demonstrates the dependence of radius on entropy for hydrogen-helium mixtures of mass 1, 3, 6, 10, and  $15 M_J$ . The radius increases rapidly with increasing entropy, and this rapid scaling is more dramatic for lower mass objects. The intersections of the radius/entropy curves with vertical lines at  $S = 10$ , 11, and 12 show the radii that may be expected for (coreless) objects at the indicated entropies. At  $S = 12$ , radii of objects from  $3M_J$  to  $15M_J$  range from  $\sim 4 R_J$  to  $\sim 3 R_J$ . At  $S = 10$ , radii range from  $\sim 2 R_J$  (at  $1M_J$ ) to  $\sim 1.5 R_J$  (at  $15M_J$ ). In an Appendix, we present an analytic fit to the radius-entropy-mass relation.

### 4. “HOT START”/“COLD START” SCENARIOS

#### 4.1. Initial Hot and Cold Start Conditions

Marley et al. (2007) published a set of “Hot Start” and “Cold Start” models, where the initial entropy had a tuning-fork shape as a function of mass. In their framework, the cold-start models were intended to represent the result of a core-accretion process, and the hot-start models were intended to represent objects formed via disk instability.

We calculate a broad range of models, from extremely hot (high-entropy, large radius) ones near the limit of gravitationally-bound stability through several relatively cold models that might represent possible outcomes of a core-accretion process. These models are summarized in Figs. 1 and 4, with the top panel of each figure showing initial entropy and the bottom panel showing initial radius as a function of mass. Figure 1 shows a total of seven families of

models. Two are the “hot” and “cold” start models from M07, shown with open and filled circles, respectively. Another is the “Hottest Start” family of models, which represents an approximate upper limit to the initial entropy that might be expected of bound objects that form via a disk-instability scenario. The other four all represent core-accretion scenarios, with various initial entropies, accretion rates, and atmospheric properties. All these models assume that accretion flows onto an initial protoplanet of low mass, with a given starting entropy. Accretion proceeds with newly-accreted material always at the specific entropy of the gas that has already accreted, which is itself slowly cooling in accordance with the atmospheric boundary condition. Our accretion models have the following properties:

- The “Acc:  $3 \times 10^{-5}$ ” models begin at an entropy of 9.8, and accrete material at  $3 \times 10^{-5} M_J/\text{yr}$ , similar to the assumed accretion rate in M07. The Burrows et al. (1997) atmospheric boundary condition is assumed. Forming a  $1-M_J$  object takes  $\sim 3 \times 10^4$  years.
- The “Acc:  $10^{-6}$ ” models are identical to the “Acc.  $3 \times 10^{-5}$ ” ones, except accretion proceeds at  $1 \times 10^{-6} M_J/\text{yr}$ , a factor of 30 slower.
- The “Acc:  $10^{-6}$ , lower S” models are identical to the “Acc.  $10^{-6}$ ” ones, except the initial entropy is 8.9 instead of 9.8.
- The “Acc:  $10^{-6}$ , Z:  $10^{-2}$ ” models are identical to the “Acc.  $10^{-6}$ ” ones, except the atmosphere boundary condition is for  $10^{-2}$ -solar metallicity. The reduced atmospheric opacity allows cooling to proceed more rapidly.

The entropy (top) and radius (bottom) panels of Fig. 1 also show several isochrones, corresponding to the “Hottest Start” models at various stages of evolution, at 0, 1, and 10 Myr, and at 1 Gyr. Interestingly, the “Hottest Start” 1-Myr isochrone is quite similar to the Marley et al. hot start models (“M07 Hot Start”).

Note that the Marley et al. curves for hot and cold models nearly converge at  $1 M_J$ , and diverge progressively more with increasing mass, leading to the tuning-fork shape seen in Fig. 1. The lower track (“M07 Cold Start”) decreases with time because  $10-M_J$  objects take longer to form than  $1-M_J$  objects, so the already-accreted gas has longer to cool. Although the Marley et al. core-accretion models and the “Acc:  $3 \times 10^{-5}$ ” models nominally have the same accretion rate, the entropy of the Marley et al. models clearly decreases with time, leading to the downward slope towards higher-mass objects (which take longer in forming), whereas the “Acc:  $3 \times 10^{-5}$ ” models’ initial entropy curve is nearly flat from  $1-10 M_J$ ; this difference might be attributable to the opacities and boundary conditions used.

The upshot of Fig. 1 – particularly of the radius panel – is that there is a very dramatic difference in the initial properties of “Hot Start” and of “Cold Start” models. Newly-formed cold-start models are predicted to have radii in the  $\sim 1.1-1.7-R_J$  range, whereas newly-formed hot-start models might have initial radii of more than  $3 R_J$ . Of course, since the core-accretion process might take of order millions of years and the disk-instability process is orders of magnitudes faster, the newly-formed objects under one scenario might correspond to a stellar age that is different by several million years from the newly-formed objects under the other formation scenario (Baraffe et al. 2002; Fortney et al. 2005).

It is also worthwhile to keep in mind that planet formation models generally predict non-monotonic evolution of luminosity during the formation process, with one or more large spikes in luminosity (e.g., Hubickyj et al. 2005; Bromley & Kenyon 2011). Our models begin (i.e., have  $t = 0$ ) when the final mass assembly is complete. Although the very early evolution of still-forming planets might contain interesting diagnostic observables, we do not explicitly calculate this process, and our models, therefore, do not predict observables for this (comparatively brief) portion of planetary evolution.

#### 4.2. Evolution of Radius, Temperature, and Entropy

We track the evolution of a broad range of models, from “Hot Start” to “Cold Start,” through an age of 1 Gyr. Figure 4 portrays our set of initial conditions (i.e., initial entropies and radii) for each mass. The large red and blue circles in Fig. 4 indicate our “Hot Start” and “Cold Start” models, which roughly trace the hottest and coldest starts shown in Fig. 1. The medium-sized yellow and green dots represent our variants of the M07 “Hot Start” and “Cold Start” models.

Figure 5 depicts the evolution of specific entropy (top panel), radius (middle panel), and effective temperature (bottom panel) for our Hot Start and Cold Start models. Evolution curves are shown for a range of masses (1, 2, 5,  $10 M_J$ ). We also calculated the evolution of objects modeled after the M07 hot and cold starts (not shown). The qualitative behavior of the evolutionary trajectories of both our hot-/cold-start models and those of M07 is the same. At early times, objects that start hot are much larger and have much higher effective temperatures than objects of equivalent mass that start cold. As “Hot Start” (red) and “Cold Start” (blue) objects of the same mass evolve, their entropies, radii, and effective temperatures asymptotically converge. The convergence seen in Fig. 5 is more rapid at lower masses for two reasons: (1) lower mass objects evolve more quickly, and (2) our initial difference between hot and cold models is smaller for lower mass objects (similar to M07, though our hot/cold models encompass a somewhat larger range). Within a few hundred million years, the memory of the initial conditions has been

lost even for  $10M_J$  objects. At early times, however, the difference is quite stark for more massive objects ( $5, 10 M_J$ ), where the initial radius and effective temperature are each a factor of  $\sim 2$  larger for “Hot Start” models than for “Cold Start” ones. These large differences in size (and, therefore, surface gravity) and effective temperature lead to striking differences in photometry and spectra (as noted by M07 and Fortney et al. 2008), and are discussed in §4.3.

The difference between a “Hot Start” model and a “Cold Start” model may be thought of as a time difference ( $\Delta t$ ) – the horizontal offset in Fig. 5 between the red and blue curves of equal mass. As objects reach ages comparable to or larger than this  $\Delta t$ , it becomes progressively more difficult to distinguish observationally between formation scenarios, on the assumption that these are the only formation conditions possible, an assumption that we revisit in §5.

#### 4.3. Spectral Evolution

The differences in entropy, radius, and effective temperature between “Hot Start” and “Cold Start” models translate into differences in spectra and broad-band magnitudes. In order to compute spectra, we assume various atmospheres. In particular, we consider four atmosphere types from Burrows et al. (2011): hybrid clouds at solar metallicity (our “fiducial” atmospheres); hybrid clouds at  $3\times$  solar metallicity; cloud-free atmospheres at solar metallicity; and cloud-free at  $3\times$  solar metallicity. Our planets are modeled as isolated objects, assumed to be in radiative equilibrium, and their emergent spectra are calculated with the line-by-line radiative transfer code COOLTLUSTY (Hubeny et al. 2003; Burrows et al. 2006).

Figure 6 shows spectra as a function of mass and age for our fiducial (i.e., hybrid clouds at solar metallicity) “Hot Start” and “Cold Start” scenarios. The red and blue (hot and cold) curves in Fig. 6 correspond to the large red and blue circles, respectively, in Fig. 4. Spectra are shown (assuming the source is at 10 pc) for objects of mass 1, 2, 5, and  $10 M_J$ , and at ages of 1, 3, 10, 30, and 100 Myrs (spectra become progressively dimmer at later ages). At  $1 M_J$ , hot- and cold-start models are nearly overlapping even at the earliest times. At higher masses, the strong difference between the fiducial “Hot Start” and “Cold Start” scenarios becomes apparent. At ages of a few Myr, for instance, the  $10M_J$  objects are several orders of magnitudes brighter at short wavelengths and early times if they start hot than if they start cold. If the dichotomy between initial conditions is as dramatic as in the fiducial models, then at early times there should be prominent observational differences (cf. M07; Fortney et al. 2008).

These differences in spectra imply differences in broad-band photometry. The evolution of  $J$ ,  $H$ ,  $K$ ,  $L'$ ,  $M$ , and  $N$ -band absolute magnitudes (for hybrid-clouds, solar-metallicity models) is shown in Fig. 7. At young ages, the magnitude differences range from

small ( $\sim 1$ ) at  $1M_J$  to more than 5 in some bands (e.g.,  $J$ ,  $H$ ,  $K$ ) at  $10M_J$ . As objects of a given mass evolve, their “hot-start” and “cold-start” brightnesses converge (in each band). The data in Fig. 7 are available in Table 1, and similar tables for the other three atmosphere types are available in electronic form online.<sup>3</sup>

#### 5. A CONTINUUM OF “WARM-START” PLANETS

Planet formation theory informs our understanding of the initial conditions to be expected for core-accretion and for disk-instability scenarios. However, significant uncertainties remain. Consider again the range of hot-start and cold-start conditions represented in both the entropy and radius panels in Fig. 1. A crucial assumption leading to the negative slope that is characteristic both of the Marley et al. core-accretion models and of our own is that the accretion process adds no heat, meaning that each parcel accretes only at the specific entropy of the gas that is already present. However, it is not clear that this assumption is warranted. Allowing infalling parcels to retain some of their nebular entropy would allow higher-mass core-accretion models to have *higher* initial entropy than lower-mass models, thereby potentially filling in the “Warm Start” regions of the two panels of Fig. 1.

Since we do not know *a priori* the initial entropies (and radii and temperatures) of objects that form via core accretion or via disk instability, it is useful to consider a broad range of possibilities. Indeed, if details of the accretion process that might differ from one planet to another govern the fraction of nebular entropy that is incorporated into the planet, then considering a broad range of possible initial entropies might be essential to reflect not just our current ignorance, but also the range of actual initial conditions from which different newly-formed planets in our galaxy begin their evolution.

Figure 4 summarizes our framework for treating a spectrum of initial conditions. At each of 1, 2, 5, and  $10 M_J$ , we show a range of initial entropies (with different models spaced by 0.25 units): 8.75 to 10.5 at  $1M_J$ , 8.5 to 11.25 at  $2M_J$ , 8.25 to 12.25 at  $5M_J$ , and 8 to 13 at  $10M_J$ . As discussed previously (§4.1), the large red/blue circles indicate our hot/cold models and the medium-sized yellow/green circles indicate the M07 hot and cold models. These particular choices for hot and cold models merely represent four values (at each mass) in a continuum of possibilities. The range of initial entropies in Fig. 4 corresponds to a range of initial radii:  $\sim 1.4$ - $3.3 R_J$  at  $1M_J$ ,  $\sim 1.3$ - $3.0 R_J$  at  $2M_J$ ,  $\sim 1.2$ - $3.6 R_J$  at  $5M_J$ , and  $\sim 1.1$ - $4.2 R_J$  at  $10M_J$ .

##### 5.1. A Dramatic Spread in Brightnesses and Spectra

<sup>3</sup> The model spectra presented in this paper are available in electronic form (at spectral resolution  $\approx 204$ ) at <http://www.sns.ias.edu/~dave/> and at <http://www.astro.princeton.edu/~burrows/>.

At a given age, models that start with different initial entropies can have very different brightnesses. For example, Fig. 9 shows the evolution of the  $K$ -band absolute magnitudes of the models denoted by dots in Fig. 4. At each of four different masses (1, 2, 5, and 10  $M_J$ ), the evolution of  $K$ -band brightnesses is shown for a range of initial entropies. As seen previously in Fig. 7, the memory of the initial conditions fades as objects evolve. At a given mass and age there is a range of possible  $K$ -band absolute magnitudes, depending on the initial entropy. Cold-start and warm-start planets of higher-mass ( $\gtrsim 5 M_J$ ) maintain relatively constant  $K$ -band absolute magnitude during their early evolution. At 5  $M_J$ , the near-constant brightness phase lasts for  $\lesssim 10$  Myr, and at 10  $M_J$ , this phase lasts for several tens of Myr. Model planets that begin with relatively high entropy are significantly brighter in the early stages and evolve much faster, not experiencing the early-evolution plateaus in brightness that cooler-start models do.

Figure 10 summarizes the spread in  $K$ -band brightness as a function of initial entropy, initial radius, mass, and age. In each panel, the ordinate indicates the increase in entropy relative to the coldest-start case (for the appropriate mass) depicted in Fig. 4. The corresponding initial radius scale for each is shown on the right  $y$ -axis as  $\Delta R_{\text{init}}$ , the increase in initial radius relative to the coldest-start case. The uneven spacing of  $\Delta R_{\text{init}}$  results from the fact that radius grows faster than linearly with entropy (see Fig. 3). The color indicates the difference between the  $K$ -band magnitude at the given entropy and the  $K$ -band magnitude for the coldest-start case. Coldest start cases have initial specific entropies of 8.75, 8.5, 8.25, and 8, and initial radii of 1.42, 1.32, 1.24, and 1.14  $R_J$ , for masses of 1, 2, 5, and 10  $M_J$ , respectively. At higher initial entropies, planets are from  $\sim 4.5$  magnitudes (at Jupiter’s mass) to  $\sim 9$  magnitudes (at 10  $M_J$ ) brighter than the corresponding coldest-start cases. As planets age, the change in  $K$ -band absolute magnitude relative to the coldest start case approaches zero. More massive objects exhibit greater differences in brightness between hottest- and coldest-start cases, and maintain these differences for significantly longer. At 1  $M_J$ , differences in brightness fade to less than a single magnitude by  $\sim 10$  Myr, even for the hottest start. At 10  $M_J$ , it takes several hundred Myr for the  $K$ -band magnitude difference between a hottest-start and a coldest-start planet to reach 1 mag. Of course, at several hundred Myr, even 10- $M_J$  planets are extremely dim in the  $K$  band. At longer wavelengths (e.g.,  $M$  and  $N$  bands), cool objects such as  $\sim 1$ -Gyr old 10- $M_J$  planets are still brighter than absolute magnitude 15 (not shown).

It is instructive to examine the evolution of the full spectral energy distribution (SED) of model planets as a function of mass and initial entropy. Figure 11 shows the full spread in  $K$ -band absolute magnitude (from the hottest-start to the coldest-start models in Fig. 4) for each of 6 bands, from  $J$  through  $N$ . At all four planet masses shown (1, 2, 5, and 10  $M_J$ ), the

difference in absolute magnitude is greatest in the  $K$  band (which is why we presented  $K$ -band evolution plots in Figs. 9 and 10). The spread in magnitudes is smallest in  $M$  band, where at 1  $M_J$  the difference between the hottest-start and coldest-start models is only  $\approx 1.5$  mags, even very early after “formation” (at 1 Myr). The relatively small differences in brightness between hottest and coldest models at  $M$  and  $N$  bands are in large part because these bands are in the Rayleigh-Jeans tail of a planet’s SED. As a result, the brightness in these bands is roughly proportional to effective temperature, which varies by no more than a factor of a few at early times, and significantly less at late times (see Fig. 5).

## 5.2. The Effect of Atmosphere

It is worthwhile to consider the effect of different atmosphere types (discussed in §4.3) on observables. Equal-mass objects with identical initial entropy can have very different colors depending on their atmospheric properties. Figure 8 provides an illustrative example of these differences, for a very hot start (initial entropy of 13) 10- $M_J$  model. The ordinate represents the difference in magnitude, as a function of age, between each of four atmosphere types (hybrid clouds, solar metallicity; hybrid clouds,  $3\times$  solar metallicity; cloud-free, solar metallicity; cloud-free,  $3\times$  solar metallicity; these are the four atmospheres of Burrows et al. 2011) and our fiducial atmosphere (hybrid clouds, solar). In  $J$  band, differences start small, but by late times the cloud-free solar models are two magnitudes fainter than the fiducial models, and 3 magnitudes fainter than the cloud-free  $3\times$  solar models. In  $K$  band, the differences between some models and others grow to more than 3 magnitudes. In  $N$  band, by contrast, the differences between cloudy and cloud-free models begin as moderate ( $\sim 1$  magnitude) and slowly decrease with age.

Another perspective on the effect of atmosphere type is provided in Fig. 12, which presents the evolution of the spread in absolute magnitude as a function of atmosphere type and spectral band for 5  $M_J$  planets. The four panels, representing the four different atmosphere types, look broadly similar, with the largest differences between hottest and coldest planets generally occurring in  $H$  and  $K$  bands. However, there are some quantitative and qualitative differences among the four panels. At solar metallicity, both the cloudy and the cloud-free models exhibit the largest hot-cold differences in  $K$  band ( $\sim 8$  magnitudes at early times), whereas at  $3\times$  solar metallicity  $H$  and  $K$  bands have approximately equal hot-cold differences ( $\sim 7$  magnitudes at early times). For all four atmospheres,  $M$  band shows the smallest hot-cold difference throughout the 1 Gyr of evolution displayed. A key result shown in Fig. 12 is that the effect of atmosphere type on the spread in absolute magnitude is not nearly so strong as the effects of changes in mass, age, or initial entropy, but spectra can nonetheless differ by several magnitudes depending upon atmospheric properties.

One can view Figs. 9-12 in a forward sense. If we know the age, mass, initial entropy, and atmosphere of a model, these figures and associated tabulated data tell us the absolute magnitude in each of 6 photometric bands in the infrared. However, this information is probably more useful when viewed in an inverse sense. For comparing these models with data, the magnitudes or spectra will be the observed quantities, and one will try to make inferences about the properties of the object. These properties include the same parameters listed for the forward problem: age (about which there might be some prior constraints from either the star or its environment), mass, initial entropy, and atmosphere type. By checking which models reasonably match observed data, we might hope to find contours in a multidimensional parameter space that rule in or rule out possible models. In this way, we may use data to infer the initial entropies of observed objects. Note that an exploration of our model space indicates that the thicker clouds employed in the models of Currie et al. (2011) and Madhusudhan et al. (2011) seem to be essential for finding self-consistent (coeval) models of planets b, c, and d in the HR8799 system.

One contour that appears to be available for the HR8799 system is the stellar age. Marois et al. (2008) argue that several lines of evidence suggest that the system has an age in the range 30-160 Myr. Moya et al. (2010) find that asteroseismological data imply an age closer to 1 Gyr. However, if the planets were 1 Gyr old, their luminosities would imply masses large enough to render the system dynamically unstable (Fabrycky & Murray-Clay 2010; Moro-Martín et al. 2010). Furthermore, Zuckerman et al. (2011) find that HR8799’s probable association with a nearby group suggests an age of  $\sim 30$  Myr. We therefore assume, for now, that the objects have ages in the range originally identified by Marois et al. (2008). The fourth planet found in the system, planet e, was recently discovered in  $K_s$  and  $L'$  band observations by Marois et al. (2010). Marois et al. find that the planet’s luminosity suggests a mass of 7-10  $M_J$  if its age is in the range 30-60 Myr. We tried to fit the photometry (the absolute magnitudes in these bands are  $12.93 \pm 0.22$  and  $11.61 \pm 0.12$ , respectively) with both the AE cloud models of Madhusudhan et al. (2011) and with our own set of models. Because of the paucity of data for planet e, a range of masses, ages, initial entropies, and atmospheres are consistent with the available data. Both the Madhusudhan et al. AE cloud models and our own hybrid cloud models (hy1s and hy3s) are consistent with the data at the ages and masses suggested by Marois et al. (2010). At these ages and masses, consistency with the photometry requires significantly higher initial entropies than our coldest start scenarios. Since our cloud-free models (cf1s and cf3s) are dimmer in  $K_s$  and  $L'$  bands than the hybrid cloud models, fitting the data with the cloud-free models requires higher masses within the age-range (30-60 Myr) specified by Marois et al.

(2010). Additional photometry at other bands could break some of the present degeneracies and might rule in or rule out some atmosphere types.

## 6. CONCLUSION

Gas-giant planets are thought to form in one of two scenarios – either runaway accretion onto a rocky or icy core, or direct gravitational collapse via a Jeans-like instability triggered in the protoplanetary disk. The former process is generally thought to lead to colder (i.e., lower entropy) objects than the latter, but first-principles calculations cannot yet specify with certainty what the initial (post-formation) entropies of objects should be in the different formation scenarios, nor whether the range of entropies resulting from the different mechanisms might overlap.

We seek observational determinants of the various models for giant planet origins, including their “initial conditions.” Candidate properties that might be discriminating include metallicity, rotation rate, mass function, or orbits. Core-accretion-formed objects might generally be expected to have higher bulk metallicity than disk-instability-formed objects; and the different modes of formation might tend to lead to differences in angular momentum, typical object mass, and initial orbit. A wrinkle associated with the idea of using rotation rate as a discriminant has to do with the fact that, for 10  $M_J$  and slightly more massive objects, a deuterium-burning phase occurs a few million years post-formation. This phase delays the evolutionary shrinkage, and when it has completed objects cool and shrink rapidly. It is conceivable that there is a signature of this rapid shrinkage embedded in the rotation rates of these objects, where massive objects burning deuterium might appear to be rotating anomalously slowly, and conservation of angular momentum might cause a spin-up in the post-deuterium stages. But without knowing precisely the initial total angular momentum budget of a massive planet, it is unclear how such a signature could be interpreted.

However, more direct signatures involve broadband colors and spectra. We have presented a large suite of evolutionary models of non-irradiated gas-giant planets, which are publicly available in electronic form. Our models span a range of “initial conditions,” with masses ranging from 1 to 15 times Jupiter’s, entropies ranging from 8 to 13 Boltzmann constants per baryon, four different atmosphere types, and a dense range of ages up to a gigayear. Motivated by (i) the strong preference for the core-accretion mode of gas-giant planet formation within the inner tens of AU, (ii) the recent observations of several young exoplanets that seem to have been born hotter than traditional “cold start” models, and (iii) the uncertainties inherent in the current generation of both core-accretion and disk-instability models of planet formation, we introduce a set of warm-start models that are at intermediate entropies between traditional “hot starts” and “cold starts.” We find the following robust conclusions:

- Objects that begin at larger radius and higher entropy can be significantly brighter in the first few million years (by 2-9 magnitudes, depending on mass and spectral band).
- These photometric differences are most prominent in  $H$  and  $K$  bands, and least in  $M$  and  $N$  bands.
- For lower-mass (1 and 2  $M_J$ ) gas giant planets, these differences fade to barely observable levels within  $\sim 10$ -30 Myr, whereas for more massive (5-10  $M_J$ ) planets, a hottest-start model can remain several magnitudes brighter than a coldest-start model in the  $K$  band for more than 100 Myr.
- Changes in atmosphere type can result in changes in brightness of a few magnitudes for some masses, ages, initial entropies, and spectral bands, but atmosphere type has less influence on a planet's emergent flux than mass, age, and initial entropy.

Some caveats remain. For one, our exploration of atmosphere types is far from complete, comprising only a single kind of cloudy atmosphere and a single cloud-free atmosphere, each at both solar and three-times solar metallicity. Other types of clouds, non-solar mixtures of elements, and nonequilibrium chemical processes could all have important effects on spectra that are not captured by our models. Perhaps more significant, we do not model in detail the formation processes, including the large spike in luminosity that might occur at very early "pre-formation" times, due to an accretion shock during either direct collapse or core accretion. Furthermore, since disk instability is thought to form planets orders of magnitude faster than the  $\sim$ several million year timescale for core accretion, there is a hidden age ambiguity that must be accounted for when our model planets are compared with observed systems. That is to say, perhaps a model that is supposed to represent disk instability should be taken to be several million years older than a model that is taken to represent core accretion. Rather than try to build this into our public models, we prefer to simply start the models at time zero with a particular initial entropy and allow others to adjust the clocks as they consider appropriate.

We hope that these models will prove to be useful in diagnosing observed young planets. By comparing data to model atmospheres, one can infer the initial, post-formation conditions of gas-giant planets. Eventually, this type of analysis might constrain planet formation mechanisms by, for instance, quantifying how much entropy nebular gas retains as it accretes onto a core. In this way, models such as those in this paper contribute toward developing a coherent picture of the evolution of planetary systems, from their formation through the epochs when we observe them.

We thank Scott Kenyon for helpful conversations and for sharing models of giant planet formation. We thank Kevin Heng, Jack Lissauer, Peter Bodenheimer, Morris Podolak, Ivan Hubeny, Sean Raymond, Madhu Nikku, and Jason Nordhaus for useful discussions. We also thank an anonymous referee for helpful comments and suggestions. The authors would like to acknowledge support in part under NASA ATP grant NNX07AG80G, HST grants HST-GO-12181.04-A and HST-GO-12314.03-A, and JPL/Spitzer Agreements 1417122, 1348668, 1371432, and 1377197. DSS acknowledges support from NSF grant AST-0807444. Models can be found at <http://www.astro.princeton.edu/~burrows/> and <http://www.sns.ias.edu/~dave/>.

## REFERENCES

- Baraffe, I., Chabrier, G., Allard, F., & Hauschildt, P. H. 2002, *A&A*, 382, 563
- Beuzit, J.-L., Feldt, M., Dohlen, K., Mouillet, D., Puget, P., Wildi, F., Abe, L., Antichi, J., Baruffolo, A., Baudoz, P., Boccaletti, A., Carillet, M., Charton, J., Claudi, R., Downing, M., Fabron, C., Feautrier, P., Fedrigo, E., Fusco, T., Gach, J.-L., Gratton, R., Henning, T., Hubin, N., Joos, F., Kasper, M., Langlois, M., Lenzen, R., Moutou, C., Pavlov, A., Petit, C., Pragt, J., Rabou, P., Rigal, F., Roelfsema, R., Rousset, G., Saisse, M., Schmid, H.-M., Stadler, E., Thalmann, C., Turatto, M., Udry, S., Vakili, F., & Waters, R. 2008, in *Society of Photo-Optical Instrumentation Engineers (SPIE) Conference Series*, Vol. 7014, *Society of Photo-Optical Instrumentation Engineers (SPIE) Conference Series*
- Boss, A. P. 2000, *ApJ*, 536, L101
- . 2007, *ApJ*, 661, L73
- . 2010, *ApJ*, 725, L145
- Bowler, B. P., Liu, M. C., Dupuy, T. J., & Cushing, M. C. 2010, *ApJ*, 723, 850
- Bromley, B. C. & Kenyon, S. J. 2011, *ApJ*, 731, 101
- Burrows, A., Guillot, T., Hubbard, W. B., Marley, M. S., Saumon, D., Lunine, J. I., & Sudarsky, D. 2000, *ApJ*, 534, L97
- Burrows, A., Heng, K., & Nampaisarn, T. 2011, *ApJ*, 736, 47
- Burrows, A., Hubbard, W. B., Lunine, J. I., & Liebert, J. 2001, *Reviews of Modern Physics*, 73, 719
- Burrows, A., Hubeny, I., Budaj, J., & Hubbard, W. B. 2007, *ApJ*, 661, 502
- Burrows, A., Marley, M., Hubbard, W. B., Lunine, J. I., Guillot, T., Saumon, D., Freedman, R., Sudarsky, D., & Sharp, C. 1997, *ApJ*, 491, 856
- Burrows, A., Sudarsky, D., & Hubeny, I. 2006, *ApJ*, 650, 1140
- Chabrier, G. & Baraffe, I. 2000, *ARA&A*, 38, 337
- Chabrier, G., Baraffe, I., Allard, F., & Hauschildt, P. H. 2005, *ArXiv Astrophysics e-prints*
- Crepp, J. R. & Johnson, J. A. 2011, *ApJ*, 733, 126
- Currie, T., Burrows, A., Itoh, Y., Matsumura, S., Fukagawa, M., Apai, D., Madhusudhan, N., Hinz, P. M., Rodigas, T. J., Kasper, M., Pyo, T., & Ogino, S. 2011, *ApJ*, 729, 128
- Dodson-Robinson, S. E., Veras, D., Ford, E. B., & Beichman, C. A. 2009, *ApJ*, 707, 79
- Fabrycky, D. C. & Murray-Clay, R. A. 2010, *ApJ*, 710, 1408
- Fischer, D. A. & Valenti, J. 2005, *ApJ*, 622, 1102
- Fortney, J. J., Marley, M. S., Hubickyj, O., Bodenheimer, P., & Lissauer, J. J. 2005, *Astronomische Nachrichten*, 326, 925
- Fortney, J. J., Marley, M. S., Saumon, D., & Ladders, K. 2008, *ApJ*, 683, 1104
- Guillot, T., Santos, N. C., Pont, F., Iro, N., Melo, C., & Ribas, I. 2006, *A&A*, 453, L21
- Harris, A. W. 1978, in *Lunar and Planetary Inst. Technical Report*, Vol. 9, *Lunar and Planetary Institute Science Conference Abstracts*, 459–461
- Hinkley, S., Oppenheimer, B. R., Brenner, D., Parry, I. R., Sivaramakrishnan, A., Soummer, R., & King, D. 2008, in *Society of Photo-Optical Instrumentation Engineers (SPIE) Conference Series*, Vol. 7015, *Society of Photo-Optical Instrumentation Engineers (SPIE) Conference Series*
- Hinkley, S., Oppenheimer, B. R., Zimmerman, N., Brenner, D., Parry, I. R., Crepp, J. R., Vasisht, G., Ligon, E., King, D., Soummer, R., Sivaramakrishnan, A., Beichman, C., Shao, M., Roberts, L. C., Bouchez, A., Dekany, R., Pueyo, L., Roberts, J. E., Lockhart, T., Zhai, C., Shelton, C., & Burruss, R. 2011, *PASP*, 123, 74
- Hubeny, I., Burrows, A., & Sudarsky, D. 2003, *ApJ*, 594, 1011
- Hubickyj, O., Bodenheimer, P., & Lissauer, J. J. 2005, *Icarus*, 179, 415
- Ibgui, L., Burrows, A., & Spiegel, D. S. 2010, *ApJ*, 713, 751
- Ikoma, M., Emori, H., & Nakazawa, K. 2001, *ApJ*, 553, 999
- Ikoma, M., Nakazawa, K., & Emori, H. 2000, *ApJ*, 537, 1013
- Janson, M., Bergfors, C., Goto, M., Brandner, W., & Lafrenière, D. 2010, *ApJ*, 710, L35
- Janson, M., Bonavita, M., Klahr, H., Lafrenière, D., Jayawardhana, R., & Zinnecker, H. 2011a, *ApJ*, 736, 89
- Janson, M., Carson, J., Thalmann, C., McElwain, M. W., Goto, M., Crepp, J., Wisniewski, J., Abe, L., Brandner, W., Burrows, A., Egner, S., Feldt, M., Grady, C. A., Golota, T., Guyon, O., Hashimoto, J., Hayano, Y., Hayashi, M., Hayashi, S., Henning, T., Hodapp, K. W., Ishii, M., Iye, M., Kandori, R., Knapp, G. R., Kudo, T., Kusakabe, N., Kuzuhara, M., Matsuo, T., Mayama, S., Miyama, S., Morino, J.-I., Moro-Martín, A., Nishimura, T., Pyo, T.-S., Serabyn, E., Suto, H., Suzuki, R., Takami, M., Takato, N., Terada, H., Tofflemire, B., Tomono, D., Turner, E. L., Watanabe, M., Yamada, T., Takami, H., Usuda, T., & Tamura, M. 2011b, *ApJ*, 728, 85
- Joergens, V. 2008, *A&A*, 492, 545
- Johnson, J. A., Aller, K. M., Howard, A. W., & Crepp, J. R. 2010, *PASP*, 122, 905
- Konopacky, Q. M., Ghez, A. M., Barman, T. S., Rice, E. L., Bailey, J. I., White, R. J., McLean, I. S., & Duchêne, G. 2010, *ApJ*, 711, 1087
- Kratzer, K. M., Murray-Clay, R. A., & Youdin, A. N. 2010, *ApJ*, 710, 1375
- Kuiper, G. P. 1951, *Proceedings of the National Academy of Science*, 37, 1
- Lagrange, A., Bonnefoy, M., Chauvin, G., Apai, D., Ehrenreich, D., Boccaletti, A., Gratadour, D., Rouan, D., Mouillet, D., Lacour, S., & Kasper, M. 2010, *Science*, 329, 57
- Leconte, J., Baraffe, I., Chabrier, G., Barman, T., & Levrard, B. 2009, *A&A*, 506, 385
- Lissauer, J. J., Hubickyj, O., D'Angelo, G., & Bodenheimer, P. 2009, *Icarus*, 199, 338
- Liu, M. C., Wahhaj, Z., Biller, B. A., Nielsen, E. L., Chun, M., Close, L. M., Ftaclas, C., Hartung, M., Hayward, T. L., Clarke, F., Reid, I. N., Shkolnik, E. L., Tecza, M., Thatte, N., Alencar, S., Artymowicz, P., Boss, A., Burrows, A., de Gouveia Dal Pino, E., Gregorio-Hetem, J., Ida, S., Kuchner, M. J., Lin, D., & Toomey, D. 2010, in *Society of Photo-Optical Instrumentation Engineers (SPIE) Conference Series*, Vol. 7736, *Society of Photo-Optical Instrumentation Engineers (SPIE) Conference Series*
- Macintosh, B., Graham, J., Palmer, D., Doyon, R., Gavel, D., Larkin, J., Oppenheimer, B., Saddlemyer, L., Wallace, J. K., Bauman, B., Evans, J., Erikson, D., Morzinski, K., Phillion, D., Poyneer, L., Sivaramakrishnan, A., Soummer, R., Thibault, S., & Veran, J.-P. 2006, in *Society of Photo-Optical Instrumentation Engineers (SPIE) Conference Series*, Vol. 6272, *Society of Photo-Optical Instrumentation Engineers (SPIE) Conference Series*
- Madhusudhan, N., Burrows, A., & Currie, T. 2011, *ApJ*, 737, 34
- Marley, M. S., Fortney, J. J., Hubickyj, O., Bodenheimer, P., & Lissauer, J. J. 2007, *ApJ*, 655, 541
- Marois, C., Macintosh, B., Barman, T., Zuckerman, B., Song, I., Patience, J., Lafrenière, D., & Doyon, R. 2008, *Science*, 322, 1348
- Marois, C., Zuckerman, B., Konopacky, Q. M., Macintosh, B., & Barman, T. 2010, *Nature*, 468, 1080
- Mayer, L., Quinn, T., Wadsley, J., & Stadel, J. 2002, *Science*, 298, 1756
- . 2004, *ApJ*, 609, 1045
- McBride, J., Graham, J. R., Macintosh, B., Beckwith, S. V. W., Marois, C., Poyneer, L. A., & Wiktorowicz, S. J. 2011, *ArXiv e-prints*
- McElwain, M. W., Metchev, S. A., Larkin, J. E., Barczys, M., Iserlohe, C., Krabbe, A., Quirrenbach, A., Weiss, J., & Wright, S. A. 2007, *ApJ*, 656, 505
- Mizuno, H. 1980, *Progress of Theoretical Physics*, 64, 544
- Mizuno, H., Nakazawa, K., & Hayashi, C. 1978, *Progress of Theoretical Physics*, 60, 699

- Mordasini, C., Alibert, Y., Klahr, H., & Benz, W. 2011, *Detection and Dynamics of Transiting Exoplanets*, St. Michel l'Observatoire, France, Edited by F. Bouchy; R. Díaz; C. Moutou; EPJ Web of Conferences, Volume 11, id.04001, 11, 4001
- Moro-Martín, A., Rieke, G. H., & Su, K. Y. L. 2010, *ApJ*, 721, L199
- Movshovitz, N., Bodenheimer, P., Podolak, M., & Lissauer, J. J. 2010, *Icarus*, 209, 616
- Moya, A., Amado, P. J., Barrado, D., García Hernández, A., Aberasturi, M., Montesinos, B., & Aceituno, F. 2010, *MNRAS*, 405, L81
- Neuhäuser, R., Mugrauer, M., Seifahrt, A., Schmidt, T. O. B., & Vogt, N. 2008, *A&A*, 484, 281
- Pollack, J. B., Hubickyj, O., Bodenheimer, P., Lissauer, J. J., Podolak, M., & Greenzweig, Y. 1996, *Icarus*, 124, 62
- Quanz, S. P., Meyer, M. R., Kenworthy, M. A., Girard, J. H. V., Kasper, M., Lagrange, A., Apai, D., Boccaletti, A., Bonnefoy, M., Chauvin, G., Hinz, P. M., & Lenzen, R. 2010, *ApJ*, 722, L49
- Rafikov, R. R. 2005, *ApJ*, 621, L69
- . 2007, *ApJ*, 662, 642
- . 2011, *ApJ*, 727, 86
- Saumon, D., Chabrier, G., & van Horn, H. M. 1995, *ApJS*, 99, 713
- Saumon, D. & Marley, M. S. 2008, *ApJ*, 689, 1327
- Schneider, J., Dedieu, C., Le Sidaner, P., Savalle, R., & Zolotukhin, I. 2011, *A&A*, 532, A79
- Spiegel, D. S., Burrows, A., & Milsom, J. A. 2011, *ApJ*, 727, 57
- Stassun, K. G., Mathieu, R. D., & Valenti, J. A. 2006, *Nature*, 440, 311
- . 2007, *ApJ*, 664, 1154
- Tamura, M. 2009, in *American Institute of Physics Conference Series*, Vol. 1158, American Institute of Physics Conference Series, ed. T. Usuda, M. Tamura, & M. Ishii, 11–16
- Zuckerman, B., Rhee, J. H., Song, I., & Bessell, M. S. 2011, *ApJ*, 732, 61

TABLE 1  
EVOLUTION OF MULTI-BAND MAGNITUDES (HYBRID CLOUDS, SOLAR ABUNDANCE)

Age (Myr)	$M (M_J)$	Hot							Cold						
		$R (R_J)$	$J$	$H$	$K$	$L'$	$M$	$N$	$R (R_J)$	$J$	$H$	$K$	$L'$	$M$	$N$
1.00	1.00	1.74	15.64	15.33	13.38	12.69	11.41	10.03	1.41	18.89	19.35	18.05	15.44	13.03	12.03
1.00	2.00	1.69	13.80	12.87	11.70	11.03	10.60	9.34	1.31	18.18	18.14	17.54	14.74	12.75	11.86
1.00	5.00	1.87	11.28	10.29	9.52	9.05	9.34	8.35	1.24	17.64	17.28	17.34	14.29	12.57	11.84
1.00	10.00	2.31	9.48	8.66	8.04	7.69	8.26	7.48	1.14	17.28	16.76	17.21	14.13	12.56	11.94
2.00	1.00	1.61	16.61	16.56	14.71	13.54	11.92	10.64	1.40	19.09	19.59	18.36	15.60	13.12	12.15
2.00	2.00	1.56	14.66	13.89	12.74	11.79	11.06	9.84	1.31	18.31	18.30	17.75	14.85	12.81	11.94
2.00	5.00	1.66	12.19	11.23	10.47	9.82	9.88	8.86	1.24	17.68	17.32	17.40	14.32	12.58	11.86
2.00	10.00	1.94	10.19	9.45	8.86	8.38	8.78	8.01	1.14	17.29	16.77	17.23	14.14	12.56	11.95
3.00	1.00	1.55	17.20	17.30	15.54	14.05	12.22	11.01	1.38	19.28	19.81	18.64	15.75	13.21	12.26
3.00	2.00	1.49	15.20	14.53	13.42	12.26	11.35	10.16	1.30	18.44	18.45	17.94	14.94	12.86	12.01
3.00	5.00	1.57	12.91	11.95	11.19	10.39	10.27	9.22	1.24	17.71	17.36	17.45	14.34	12.60	11.88
3.00	10.00	1.77	10.63	9.89	9.30	8.77	9.08	8.30	1.14	17.30	16.78	17.24	14.14	12.57	11.96
5.00	1.00	1.48	18.03	18.32	16.76	14.75	12.62	11.51	1.37	19.61	20.21	19.17	16.02	13.36	12.46
5.00	2.00	1.42	16.05	15.56	14.52	12.99	11.77	10.65	1.29	18.67	18.73	18.30	15.13	12.97	12.15
5.00	5.00	1.48	13.65	12.72	11.99	11.00	10.66	9.59	1.24	17.79	17.45	17.57	14.40	12.63	11.92
5.00	10.00	1.59	11.37	10.59	9.98	9.36	9.55	8.71	1.14	17.32	16.81	17.27	14.16	12.58	11.97
7.00	1.00	1.43	18.54	18.92	17.50	15.16	12.87	11.82	1.35	19.91	20.56	19.63	16.25	13.50	12.64
7.00	2.00	1.38	16.64	16.27	15.31	13.48	12.05	10.99	1.29	18.88	18.97	18.62	15.29	13.06	12.27
7.00	5.00	1.43	14.09	13.19	12.48	11.36	10.90	9.83	1.23	17.85	17.53	17.67	14.45	12.66	11.96
7.00	10.00	1.50	12.08	11.23	10.58	9.87	9.94	9.03	1.14	17.33	16.83	17.31	14.17	12.59	11.98
10.00	1.00	1.39	19.19	19.71	18.51	15.68	13.17	12.21	1.33	20.33	21.05	20.29	16.57	13.68	12.88
10.00	2.00	1.34	17.35	17.15	16.33	14.08	12.38	11.39	1.28	19.17	19.31	19.07	15.51	13.18	12.43
10.00	5.00	1.39	14.65	13.80	13.14	11.82	11.17	10.13	1.23	17.95	17.64	17.83	14.53	12.70	12.02
10.00	10.00	1.44	12.72	11.80	11.14	10.33	10.28	9.31	1.14	17.36	16.86	17.35	14.20	12.60	12.00
15.00	1.00	1.35	19.97	20.62	19.70	16.29	13.53	12.67	1.31	20.86	21.66	21.13	16.98	13.92	13.19
15.00	2.00	1.31	18.14	18.09	17.47	14.71	12.73	11.85	1.27	19.58	19.78	19.70	15.82	13.36	12.66
15.00	5.00	1.34	15.27	14.50	13.92	12.35	11.48	10.47	1.23	18.11	17.82	18.08	14.65	12.77	12.11
15.00	10.00	1.38	13.29	12.33	11.69	10.77	10.59	9.59	1.14	17.41	16.91	17.42	14.23	12.62	12.02
20.00	1.00	1.32	20.61	21.37	20.74	16.79	13.81	13.04	1.29	21.34	22.21	21.91	17.33	14.12	13.46
20.00	2.00	1.29	18.77	18.85	18.45	15.21	13.01	12.20	1.26	19.95	20.21	20.30	16.10	13.52	12.87
20.00	5.00	1.32	15.76	15.07	14.58	12.76	11.71	10.75	1.22	18.27	17.99	18.32	14.77	12.84	12.20
20.00	10.00	1.34	13.71	12.74	12.13	11.10	10.81	9.80	1.14	17.45	16.96	17.49	14.26	12.64	12.05
30.00	1.00	1.29	21.51	22.40	22.16	17.47	14.21	13.56	1.27	21.97	22.92	22.92	17.80	14.40	13.82
30.00	2.00	1.26	19.63	19.83	19.76	15.86	13.38	12.69	1.24	20.54	20.87	21.23	16.53	13.76	13.20
30.00	5.00	1.28	16.44	15.87	15.54	13.33	12.04	11.15	1.22	18.54	18.30	18.74	14.97	12.95	12.35
30.00	10.00	1.29	14.24	13.28	12.73	11.54	11.09	10.08	1.13	17.54	17.06	17.64	14.33	12.67	12.10
50.00	1.00	1.25	22.69	23.73	24.11	18.32	14.70	14.22	1.24	23.05	24.13	24.71	18.58	14.85	14.42
50.00	2.00	1.23	20.86	21.22	21.74	16.75	13.89	13.37	1.22	21.45	21.88	22.72	17.18	14.14	13.70
50.00	5.00	1.25	17.44	17.04	17.03	14.13	12.48	11.72	1.21	19.01	18.83	19.51	15.32	13.15	12.62
50.00	10.00	1.24	14.94	14.03	13.61	12.13	11.45	10.49	1.13	17.70	17.24	17.91	14.46	12.74	12.20
100.00	1.00	1.21	24.50	25.71	27.13	19.60	15.44	15.21	1.20	24.69	25.91	27.44	19.72	15.52	15.31
100.00	2.00	1.20	22.55	23.07	24.53	17.94	14.58	14.29	1.20	22.88	23.43	25.09	18.17	14.72	14.47
100.00	5.00	1.21	18.92	18.73	19.36	15.25	13.11	12.57	1.19	19.92	19.82	20.98	15.96	13.52	13.12
100.00	10.00	1.18	15.98	15.24	15.13	13.05	11.96	11.13	1.12	18.07	17.65	18.52	14.73	12.90	12.42

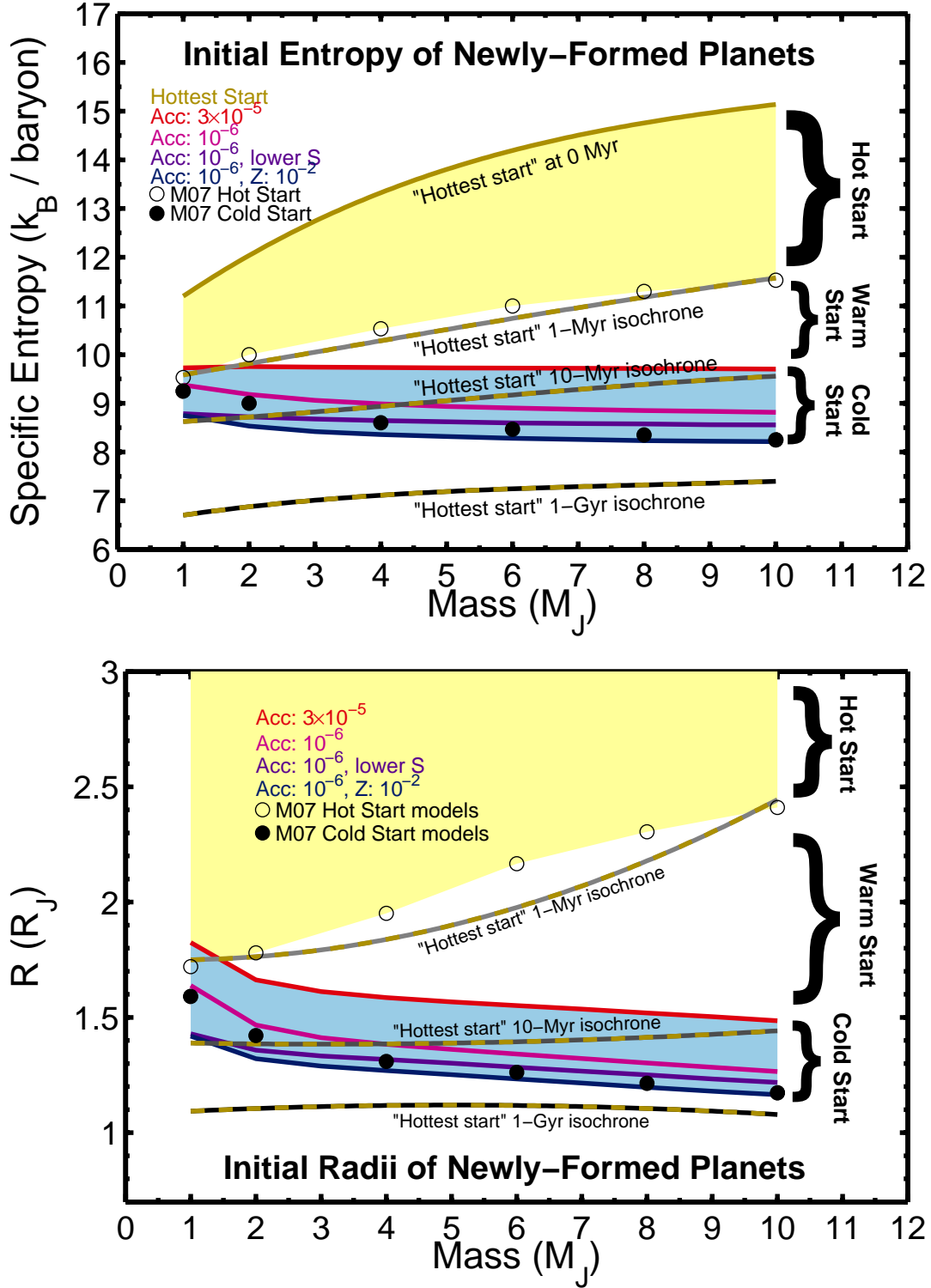


FIG. 1.— Models of specific entropy (*top*) and radius (*bottom*) of newly-formed planets. Values from M07 are shown as open (filled) circles for hot (cold) start models. Four families of core accretion models are shown (accretion rates of  $3 \times 10^{-5} M_J/\text{yr}$  to  $10^{-6} M_J/\text{yr}$ , with various metallicities and initial entropies). There is also a “Hottest start” family of models shown with extremely high initial entropies and radii. 1-Myr, 10-Myr, and 1-Gyr isochrones of the “Hottest start” model are shown; the 1-Myr isochrone is fairly similar to the Marley et al. “Hot Start” models. Representative bands are shown for cold-start (blue), hot-start (yellow), and warm-start models.

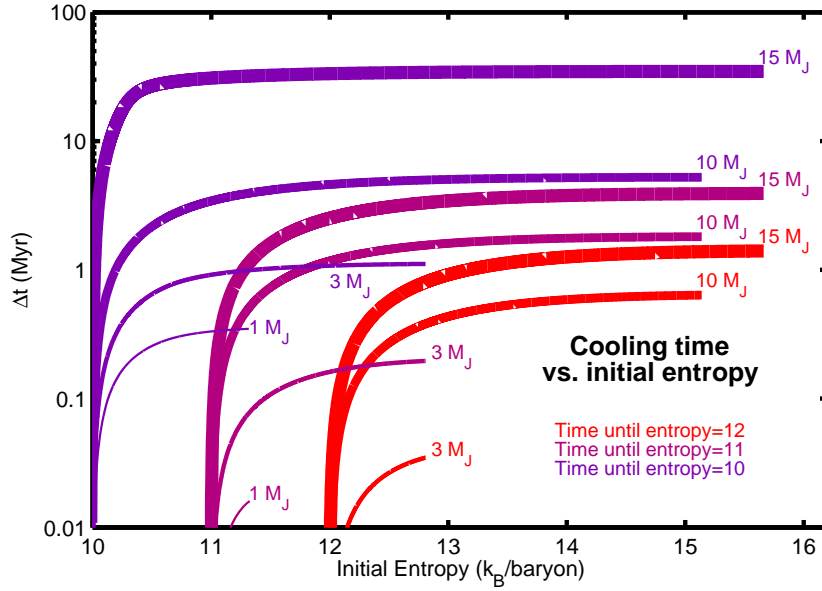


FIG. 2.— Cooling time as a function of initial entropy for Burrows et al. (1997) models, for 1, 3, 10, and 15  $M_J$ . Line thickness indicates mass, with thicker lines denoting more massive objects. Red, magenta, and blue curves have final specific entropies of 12, 11, and 10, respectively. Objects even as massive as 10  $M_J$  cool to an entropy of 12 very quickly (in less than a million years after the end of accretion), regardless of their initial entropy. Cooling to an entropy of 11 takes a factor of several longer ( $\sim 2$  Myr for 10- $M_J$  models that start very hot). Cooling to an entropy of 10 requires  $\sim 5$  Myr for 10- $M_J$  models. Cooling times are a factor of  $\sim 4$  less for 3- $M_J$  models and another factor of  $\sim 3$  less for 1- $M_J$  models.

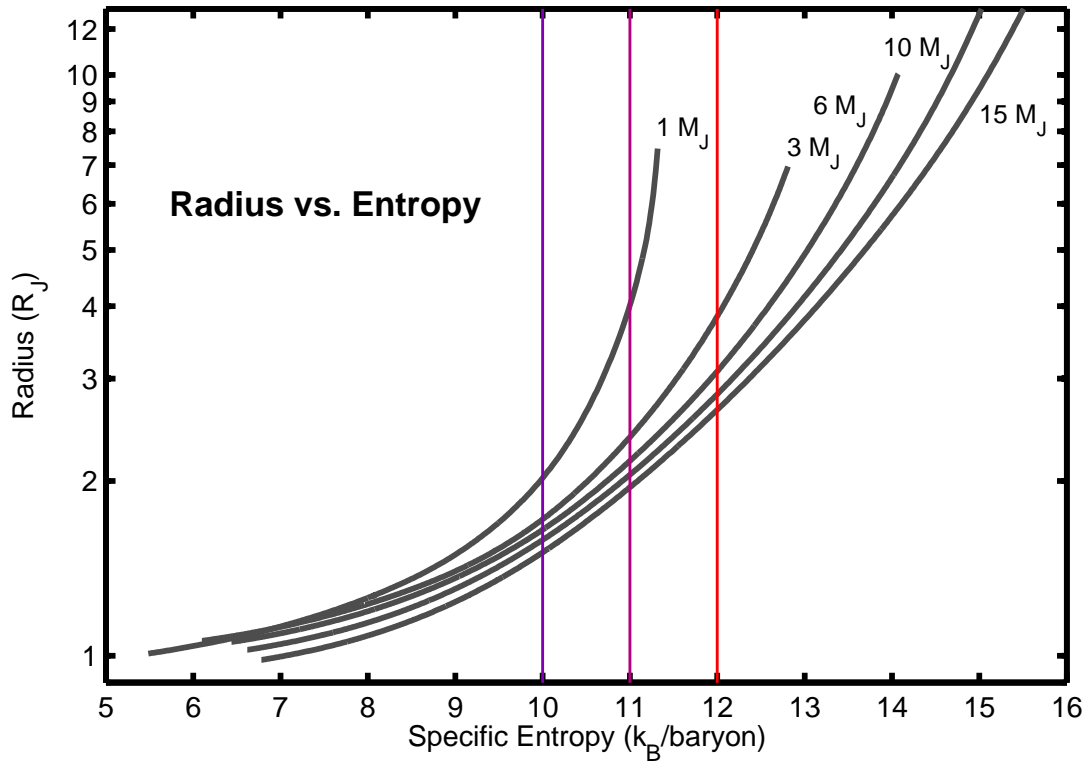


FIG. 3.— Radius vs. Entropy for objects of mass 1, 3, 6, 10, and 15  $M_J$ . Radius increases rapidly with increasing entropy, more so for lower mass objects. Vertical lines (in colors corresponding to those in Fig. 2) mark where the entropy per baryon has values of 10, 11, and 12.

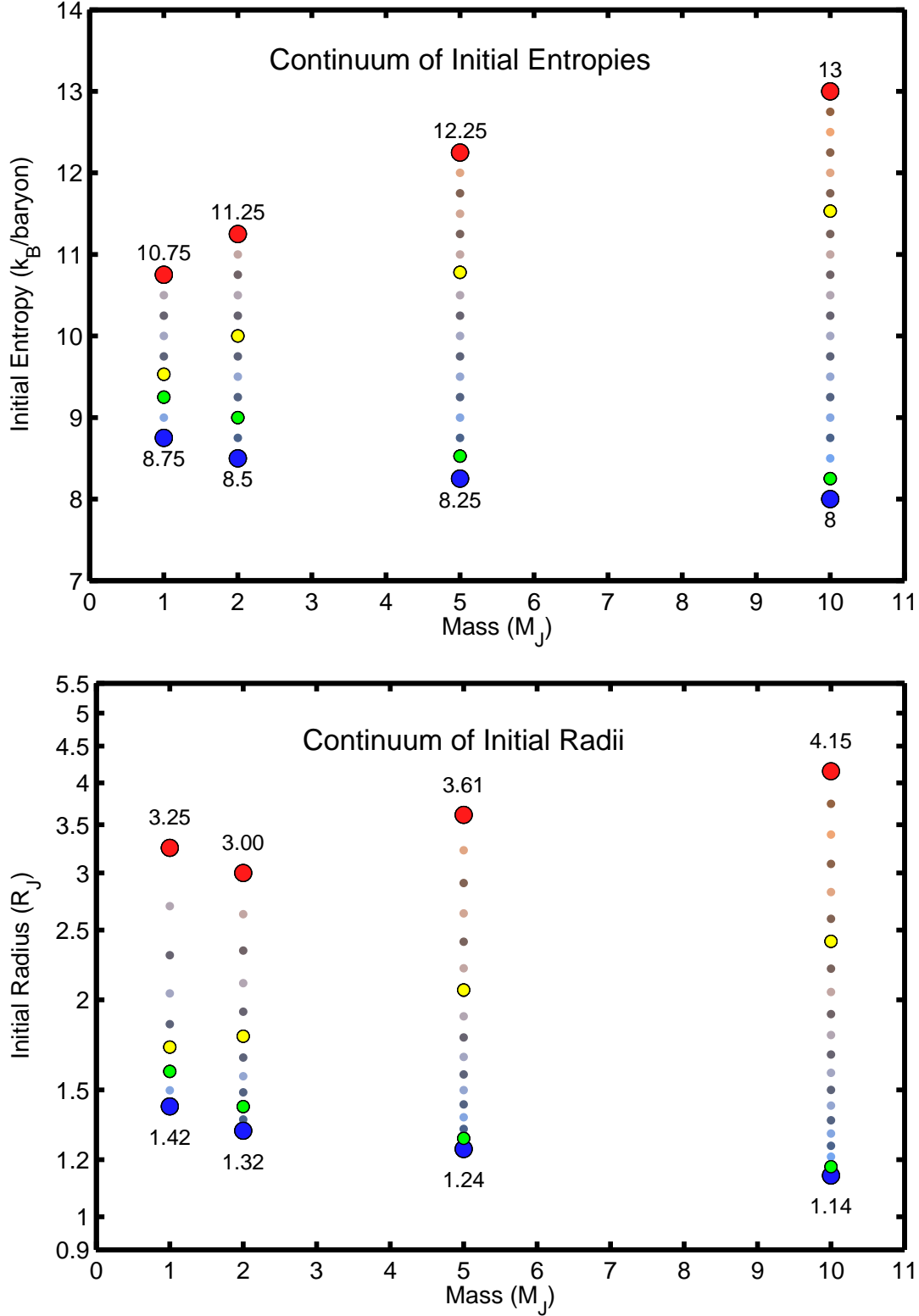


FIG. 4.— Range of initial entropies (*top*) and corresponding initial radii (*bottom*) that we employ for evolution calculations are displayed. For each of 1, 2, 5, and 10  $M_J$ , a broad set of initial entropy values (in steps of 0.25) are listed. Very large red (blue) circles indicate our “Hot Start” (“Cold Start”) scenarios. Medium-sized yellow (green) circles indicate our versions of the M07 “hot-start” (“cold-start”) models. For more massive objects, the highest and the lowest plausible entropies both become more extreme. The radii corresponding to the entropies of the top panel are shown in the bottom panel.

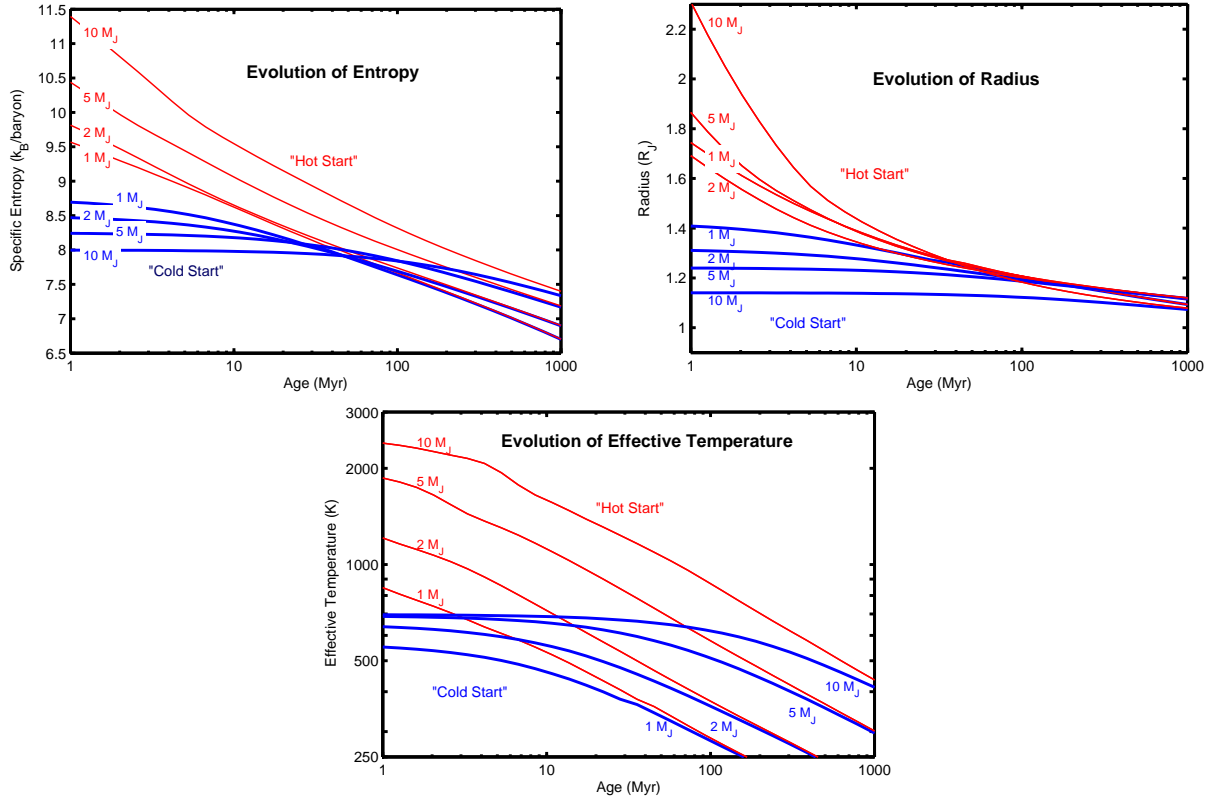


FIG. 5.— Evolution of specific entropy (*top*), radius (*middle*), and effective temperature (*bottom*), for a range of masses (1, 2, 5, 10  $M_J$ ), for a particular set of “Hot Start” (red) and “Cold Start” (blue) initial conditions, corresponding to the large red and blue dots in Fig. 4, respectively. The differences in radius and temperature between the “Hot Start” and the “Cold Start” objects is dramatic at early times, particularly for more massive objects. As “Hot Start” and “Cold Start” objects of the same mass evolve, their entropies, radii, and effective temperatures asymptotically converge, such that within a few hundred million years the memory of the initial conditions has been lost even for 10- $M_J$  objects. Lower mass objects lose memory of their initial conditions within a few to a few tens of million years.

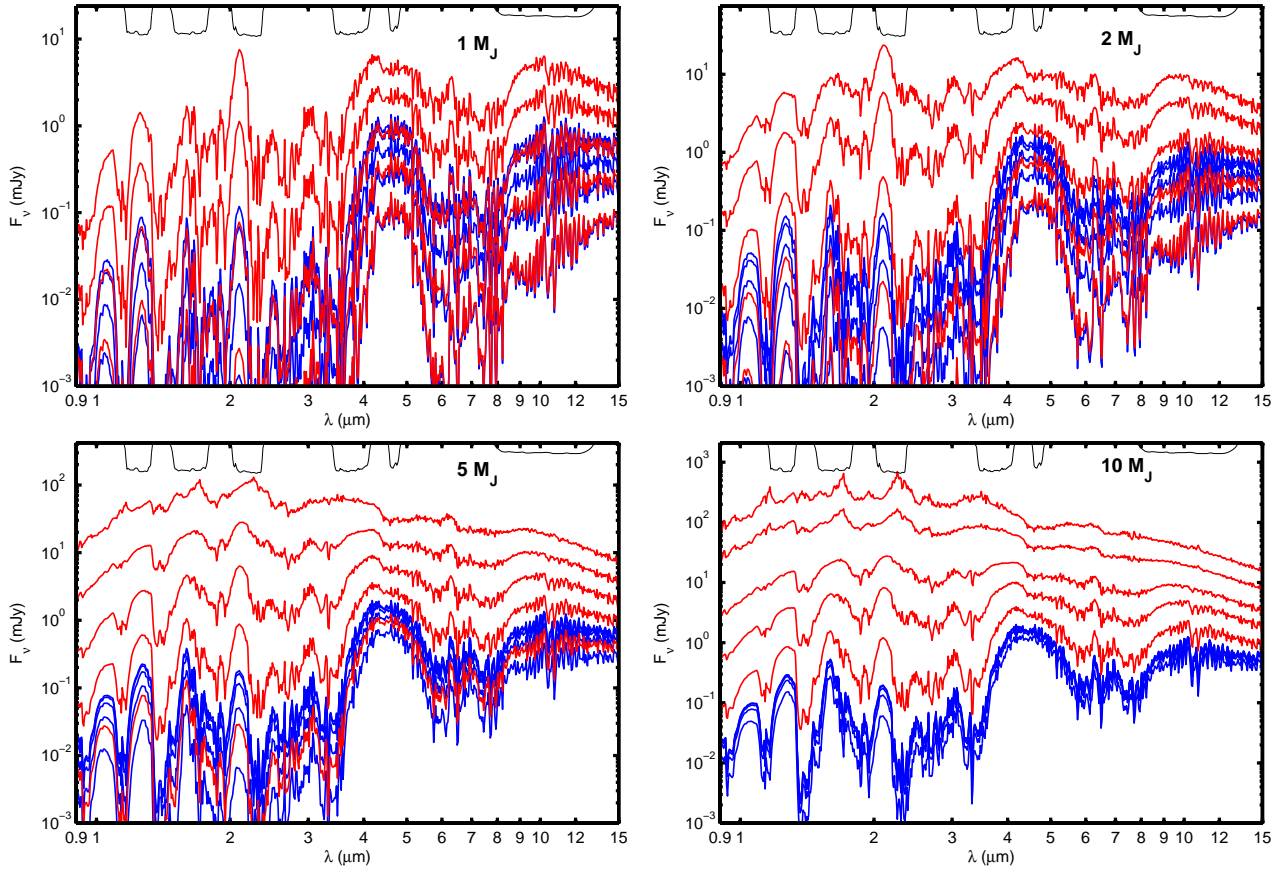


FIG. 6.— Evolution of spectra for “Hot Start” (red) and “Cold Start” (blue) models for objects with hybrid-cloudy atmospheres at solar metallicity (Burrows et al. 2011). The initial conditions correspond to the large red and blue dots in Fig. 4. Spectra are shown (assuming the source is at 10 pc) for objects of mass  $1M_J$  (top left),  $2M_J$  (top right),  $5M_J$  (bottom left), and  $10M_J$  (bottom right). In each panel, 5 spectra are shown for each initial condition, indicating isochrones of 1, 3, 10, 30, and 100 Myrs. At the top of each panel, thin black lines indicate the transmission functions for  $J$ ,  $H$ ,  $K$ ,  $L'$ ,  $M$ , and  $N$  bands.

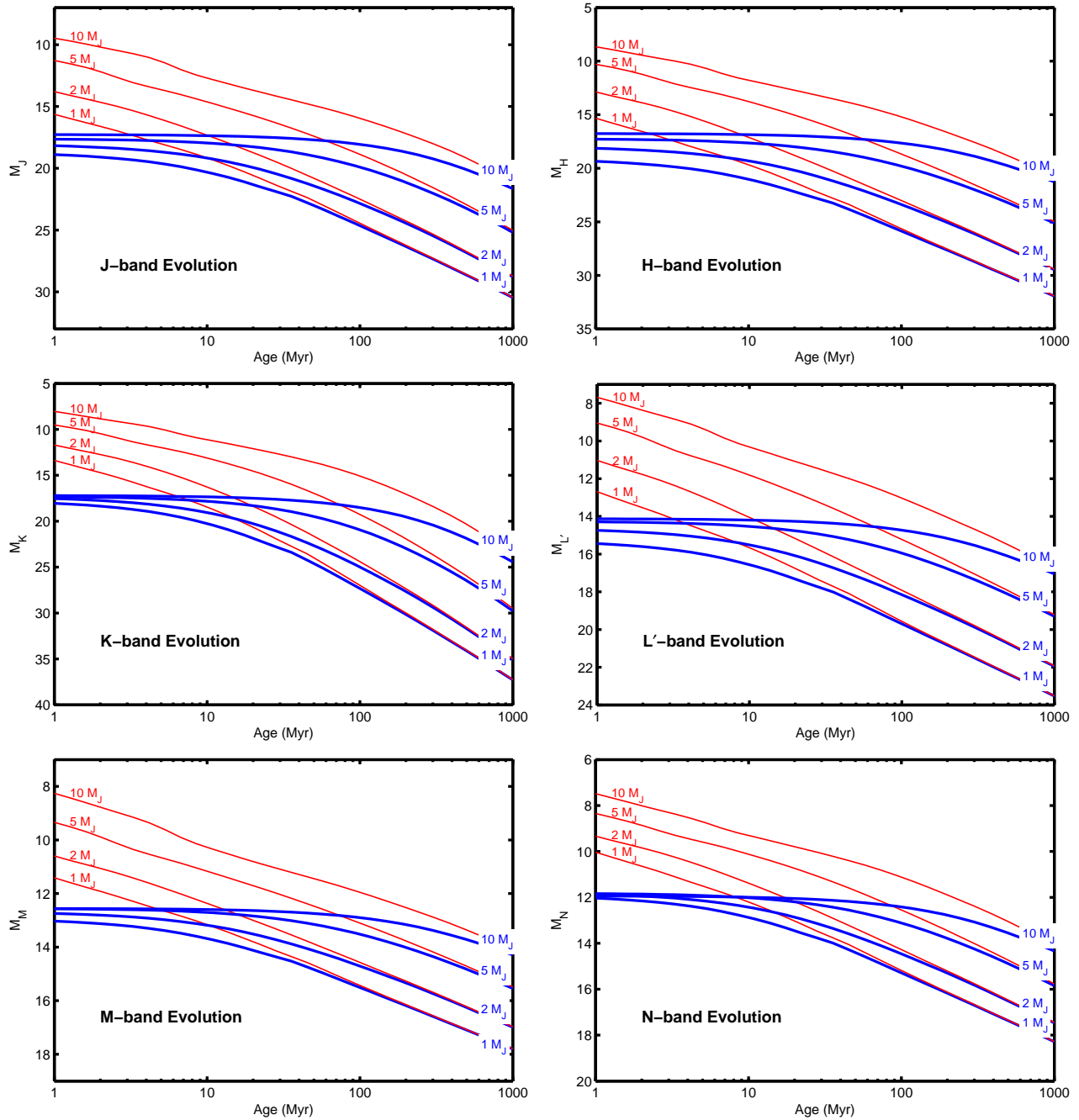


FIG. 7.— Evolution of absolute magnitudes. “Hot Start” (red) and “Cold Start” (blue) models are shown for 1, 2, 5, and  $10M_J$ . Evolutionary trajectories are shown for  $J$  (top left),  $H$  (top right),  $K$  (middle left),  $L'$  (middle right),  $M$  (bottom left), and  $N$  (bottom right) bands. Hot and cold-start models begin at very different brightnesses, but as objects age the differences quickly approach zero.

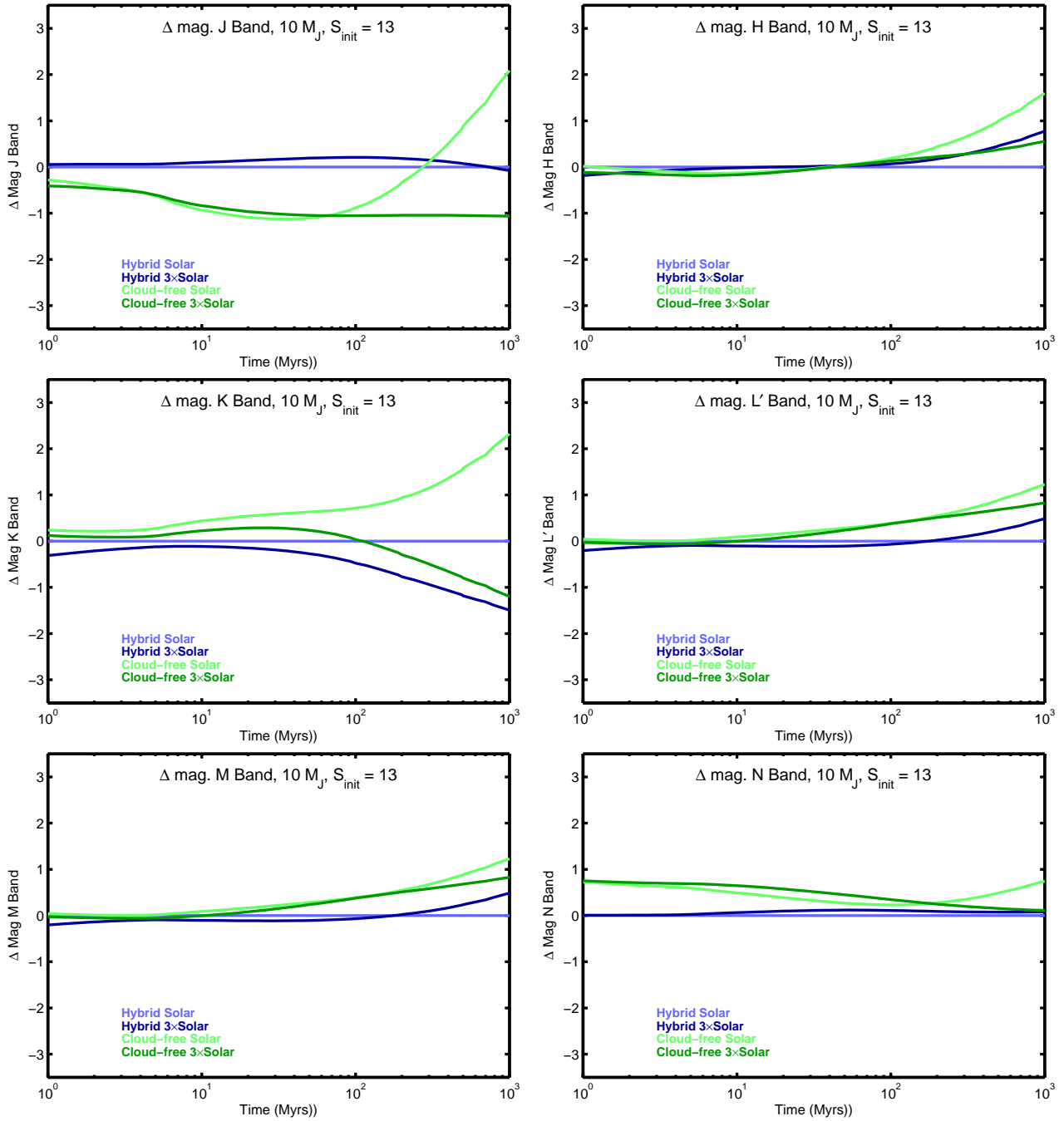


FIG. 8.— Illustrative examples of evolution of the difference in magnitude relative to the fiducial atmosphere (i.e., relative to a hybrid clouds, solar metallicity atmosphere model). This figure shows the differences for an object of mass  $10 M_J$  with initial entropy of 13. In some bands, at some ages, the differences in brightness from one atmosphere model to another (at identical object mass and initial entropy) can be several magnitudes.

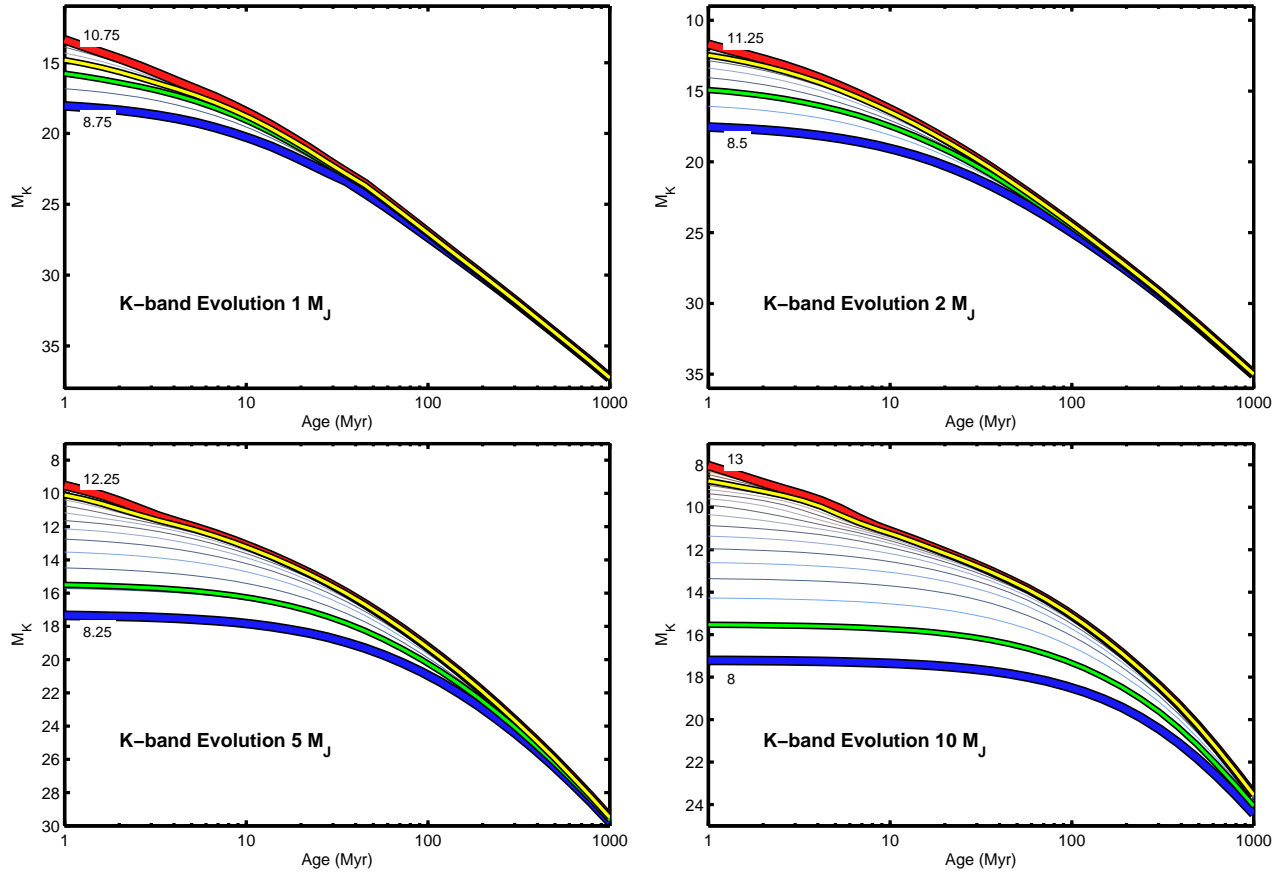


FIG. 9.— Evolution of absolute  $K$ -band magnitude for different masses and different initial entropies. Evolutionary tracks are shown for each of the models represented by dots in Fig. 4 (with corresponding colors). Thick red and blue curves represent our hottest- and coldest-start models, corresponding to the large dots of the same color in Fig. 4; medium-thick yellow and green curves similarly represent our version of the M07 “hot-start” and “cold-start” models. At each of  $1 M_J$  (top left),  $2 M_J$  (top right),  $5 M_J$  (bottom left), and  $10 M_J$  (bottom right), planets begin bright in the  $K$ -band and cool with time. Those that begin with higher initial entropy (and larger radius and higher effective temperature) are significantly brighter at early times than those that begin cooler. As objects evolve, the memory of the initial conditions fades, but at a given mass and a given age there are a range of possible  $K$ -band magnitudes, depending on the initial entropy.

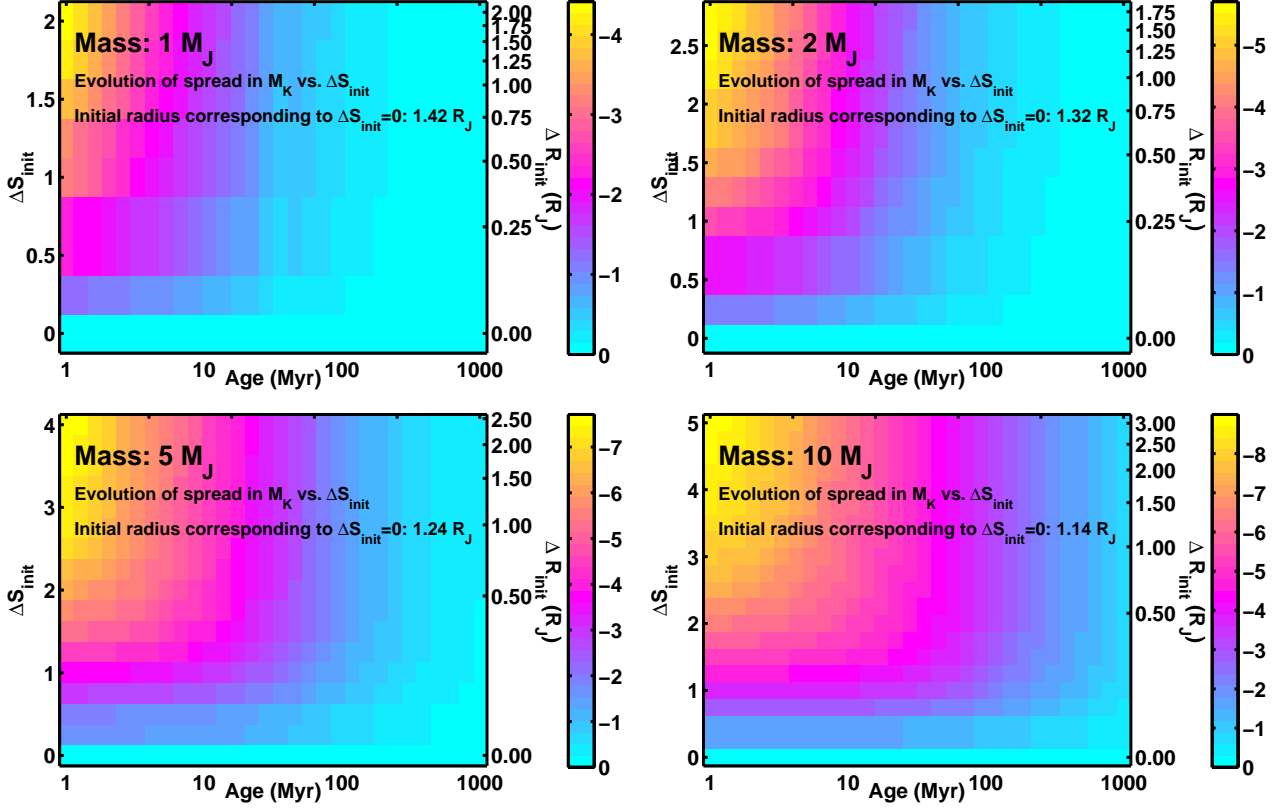


FIG. 10.— Evolution of  $K$ -band absolute magnitude as a function of initial entropy and mass. For each of four planet masses –  $1M_J$  (top left),  $2M_J$  (top right),  $5M_J$  (bottom left),  $10M_J$  (bottom right) – the change in  $K$ -band absolute magnitude relative to the corresponding “coldest start” case in Fig. 4 is shown. The coldest start cases have initial specific entropies of 8.75, 8.5, 8.25, and 8, and initial radii of 1.42, 1.32, 1.24, and 1.14  $R_J$ , for masses of 1, 2, 5, and 10  $M_J$ , respectively. The left  $y$ -axis of each panel shows the increase in specific entropy relative to the coldest start. The right  $y$ -axis of each panel shows the change in radius relative to the coldest start. At higher initial entropies (and larger initial radii), planets are brighter in the  $K$  band. As planets age, the change in  $K$ -band absolute magnitude relative to the coldest start case approaches zero. Note that each panel has an independent color stretch. More massive objects exhibit greater differences in brightness between the coldest and the hottest starts, and their differences persist for longer.

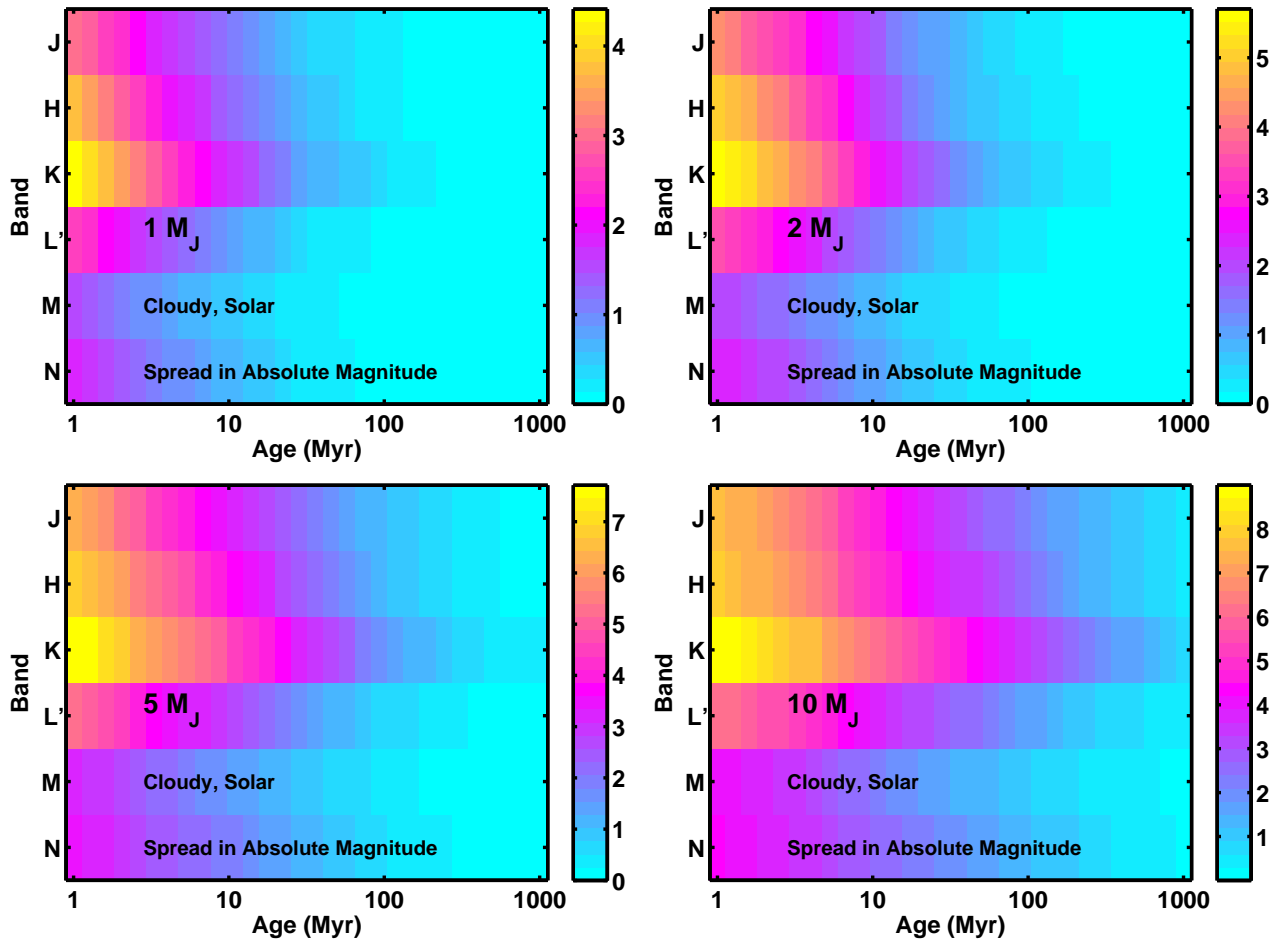


FIG. 11.— Evolution of spread in absolute magnitude as a function of mass and spectral channel. For each of four planet masses –  $1M_J$  (top left),  $2M_J$  (top right),  $5M_J$  (bottom left),  $10M_J$  (bottom right) – the difference in absolute magnitude between the coldest start and the hottest start cases in Fig. 4 is shown. The atmospheres of all objects are the hybrid cloudy models at solar metallicity from Burrows et al. (2011). Note that each panel has an independent color stretch. In all six bands, more massive objects exhibit greater differences in brightness between the coldest and the hottest starts, and their differences persist for longer. The spread in absolute magnitude is greatest at  $K$  band throughout the range of masses.

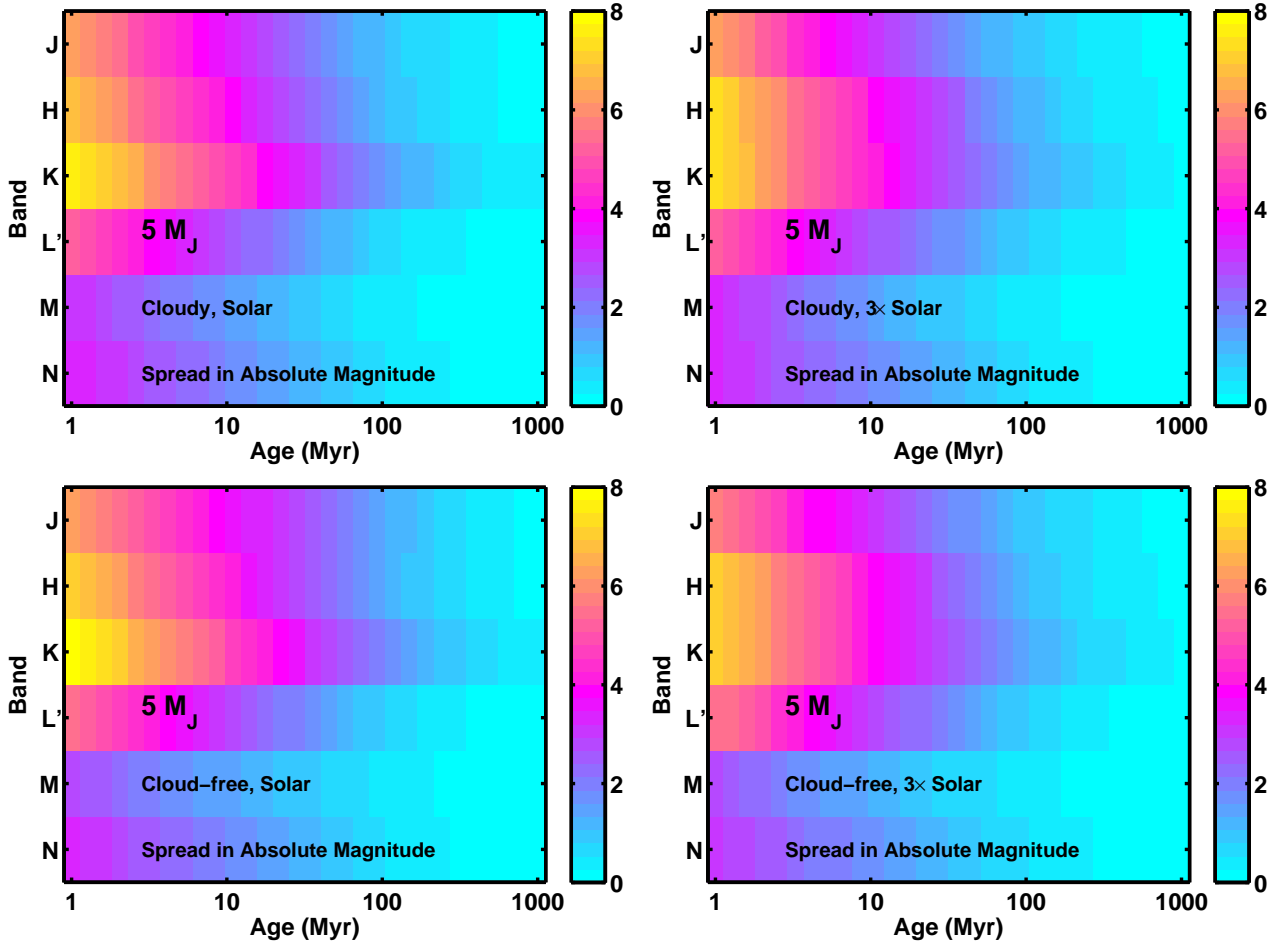


FIG. 12.— Evolution of spread in absolute magnitude as a function of atmosphere type and spectral channel. For each of four atmosphere types – cloudy at solar metallicity (*top left*), cloudy at three times solar metallicity (*top right*), cloud-free at solar metallicity (*bottom left*), cloud-free at three times solar metallicity (*bottom right*) – the difference in absolute magnitude between the coldest start and the hottest start cases in Fig. 4 is shown. Details regarding the atmosphere types are described in Burrows et al. (2011). All model planets are  $5 M_J$ . The effect of atmosphere type on the spread in absolute magnitude is not dramatic, although significant differences exist from one spectrum to another which are not apparent in this figure.

## APPENDIX

## AN ANALYTIC FIT FOR RADIUS

Here, we present a fit to the radius-entropy-mass relation that works quite well for masses between  $0.3 M_J$  and  $15 M_J$  (and for reasonable radii). Because of a distinct change in the behavior of the  $R[S, M]$  surface near  $2 M_J$ , we present two separate fits in the two domain regions. Each is an exponential of a polynomial (3rd order in  $S$  and 2nd order in  $M$ ).

For  $M \leq 2 M_J$ ,

$$\begin{aligned}
 p_{00} &= -1.27 \\
 p_{10} &= 0.5404 \\
 p_{01} &= -0.09388 \\
 p_{20} &= -0.08935 \\
 p_{11} &= 0.1549 \\
 p_{02} &= -0.3515 \\
 p_{30} &= 0.005578 \\
 p_{21} &= -0.02021 \\
 p_{12} &= 0.05055.
 \end{aligned} \tag{1}$$

Likewise, for  $M > 2 M_J$ ,

$$\begin{aligned}
 p_{00} &= 0.2273 \\
 p_{10} &= -0.03987 \\
 p_{01} &= -0.02136 \\
 p_{20} &= -0.002942 \\
 p_{11} &= 0.00655 \\
 p_{02} &= -0.001173 \\
 p_{30} &= 0.0007376 \\
 p_{21} &= -0.0005432 \\
 p_{12} &= 0.0001446.
 \end{aligned} \tag{2}$$

Then, for  $M$  in  $M_J$  and  $S$  in  $k_B$  per baryon, the following is an excellent fit to the  $R[S, M]$  function when  $R \leq 2 R_J$ :

$$\text{LogR} = p_{00} + p_{10}S + p_{01}M + p_{20}S^2 + p_{11}SM + p_{02}M^2 + p_{30}S^3 + p_{21}S^2M + p_{12}SM^2 \tag{3}$$

$$R[S, M] \approx 10^{\text{LogR}} R_J. \tag{4}$$